

AN INTEGRATED DAMAGE, VISUAL, AND RADAR ANALYSIS OF THE 2015 FOSHAN, GUANGDONG, EF3 TORNADO IN CHINA PRODUCED BY THE LANDFALLING TYPHOON MUJIGAE (2015)

LANQIANG BAI, ZHIYONG MENG, LING HUANG, LIJUN YAN,
ZHAOHUI LI, XUEHU MAI, YIPENG HUANG, DAN YAO, AND XI WANG

Damage- and visually derived tornado features, radar-derived tornado signatures, and their juxtapositions are revealed in a tropical cyclone–associated enhanced Fujita 3 (EF3) tornado.

Tropical cyclone (TC) tornadoes may contribute up to 10% of the overall fatalities and up to 0.5% of the damage caused by their parent TCs (Novlan and Gray 1974), although they are usually characterized by smaller size, lower intensity, and less

severe damage relative to midlatitude tornadoes (e.g., Smith 1965; McCaul and Hagemeyer 2016). There have been several detailed analyses that integrate damage, visual, and radar analyses of midlatitude tornadoes, revealing detailed low-level wind fields and the relationship between the condensation funnel, damage swath, and radar observations (e.g., Wakimoto et al. 2003; Atkins et al. 2014; Wakimoto et al. 2016). Whether these features of TC tornadoes are similar to or different from those of midlatitude tornadoes remains unknown. Revealing these features is important to understand tornadoes in a TC environment and to provide scientific references for landfalling TC disaster preparedness and mitigation. This study provides a detailed case review of a TC-induced tornado with the most comprehensive information ever collected in a tornado case in the history of China.

Most previous work on TC tornadoes was on either climatological statistics (e.g., Smith 1965; Hill et al. 1966; Novlan and Gray 1974; Gentry 1983; McCaul

AFFILIATIONS: BAI, MENG, L. HUANG, Y. HUANG, AND YAO—Laboratory for Climate and Ocean-Atmosphere Studies, Department of Atmospheric and Oceanic Sciences, School of Physics, Peking University, Beijing, China; YAN, LI, AND MAI—Foshan Tornado Research Center, Foshan, Guangdong Province, China; WANG—National Satellite Meteorological Center, China Meteorological Administration, Beijing, China

CORRESPONDING AUTHOR: Zhiyong Meng, zymeng@pku.edu.cn

The abstract for this article can be found in this issue, following the table of contents.

DOI:10.1175/BAMS-D-16-0015.1

In final form 26 March 2017

©2017 American Meteorological Society

For information regarding reuse of this content and general copyright information, consult the [AMS Copyright Policy](#).

1991; Verbout et al. 2007; Schultz and Cecil 2009; Moore and Dixon 2011; Edwards 2012), radar analysis (e.g., Spratt et al. 1997; McCaul et al. 2004; Rao et al. 2005), or numerical modeling (McCaul and Weisman 1996; Mashiko et al. 2009; Morin et al. 2010). TC tornadoes are quite frequent severe weather events in landfalling TC environments. Gentry (1983) found that nearly every TC of full hurricane intensity whose center crossed the U.S. coast between Brownsville, Texas, and Long Island, New York, had associated tornadoes. TC tornadoes tend to be spawned from minisupercells in the right-front (motion relative) or northeastern (Earth relative) quadrant of their parent TCs (Smith 1965; Novlan and Gray 1974; Gentry 1983; Weiss 1987; McCaul 1991) during (or after) the TCs' water-to-land transition, probably resulting from the enhancement of vertical wind shear and helicity caused by the increased surface friction (Novlan and Gray 1974; Gentry 1983) or the interaction between TCs and baroclinic westerlies (McCaul 1991). Gentry (1983) showed that TC tornadoes formed most frequently between 1200 and 1800 local standard time (LST) with a peak between 1500 and 1800 LST, and 72% of the TC tornadoes were spawned while the TC center was either still at sea or no more than 250 km inland.

China has an average of eight landfalling TCs each year (Li et al. 2004) and TC tornadoes are reported at least once a year (e.g., Huang et al. 2014; Zheng et al. 2015). Located on the southeastern coast of China, Guangdong Province has a high frequency of tornadoes with a spatial peak in the Foshan area (locations are given in Fig. 1a) (Huang et al. 2014; Fan and Yu 2015). According to our statistics, at least 19 tornadoes were reported in Foshan during 2006–15, about 53% of which were spawned in a TC environment. At around 1400 LST (LST = UTC + 8 hr) 4 October 2015, Mujigae, the strongest typhoon to land in Guangdong Province in October since 1949 (Tao et al. 2016; Yang and Gao 2016), landed in Zhanjiang, Guangdong Province (Fig. 1b). Several minisupercells developed in the northeastern quadrant of the TC circulation while the TC was making landfall. Three minisupercells separately spawned one tornado in Foshan, one tornado in Guangzhou, and one waterspout in Shanwei (the approximate locations of the three tornadoes are indicated by the red arrows in Fig. 1a).

This work presents the most detailed TC tornado damage survey so far in the literature based on the TC tornado that hit Foshan on 4 October 2015 (Figs. 1b,c). It caused four fatalities and an estimated property damage of \$29 million (Zhao et al. 2017), which accounted for 21% of the overall fatalities and 0.84% of the damage caused by its parent TC. The

most comprehensive information of a tornado case in the history of China so far was available in this event, including real-time tornado videos, photographs, an intensive radiosonde observation, radar observations, and intensive surface observations, in addition to independent ground and aerial damage surveys. The main objective of this study is to reveal the details of damage caused by a TC tornado, its low-level wind pattern, and the relationship between the condensation funnel, damage swath, and radar observations. This study provided the most detailed tornado case review in the history of China with the first-time usage of a drone in a tornado damage survey. Most previous work on tornado damages in China included only a couple of damage pictures at some spots with a rough tornado track (e.g., Lin 1995; Mou et al. 2001; Fang et al. 2009; Zheng 2009). Meng and Yao (2014) performed the most detailed damage survey analysis on the 21 July 2012 Beijing, China, tornado until now. However, they were not able to provide a map of detailed enhanced Fujita scale (EF scale) distribution along the tornado track and near-surface wind fields because of the lack of an aerial survey and any visual observations.

DATA AND METHODOLOGY. *Damage survey methodology.* The damage survey was performed for 5 days immediately after the Foshan tornado through a collaboration with Peking University, Foshan Tornado Research Center, Nanjing University, and the China Meteorological Administration. Detailed ground surveys were conducted at 17 places (Fig. 2), including Liandu (LD), Longyan (LY), Boaocheng (BAC), Shibao (SB), Xintang (XT), Jiangyi (JY), Media Industrial Zone (MIZ), Xianlong (XL), Malong Industrial Zone (MLI), Laoyue Industrial Zone (LYI), Xiaocong (XC), Dadun (DD), Jiabocheng (JBC), Dasha (DS), Happy Restaurant (HR), the highway entrance in Zhangcha (HE), and Luocun (LC). During the ground survey, a total of 1,152 photographs were taken. Detailed information of damaged structures, fallen trees, and debris was collected. An aerial survey was performed along the damage swath from LD to JBC using a quadcopter drone equipped with a 1080p video camera and flown at about 100 m above ground level (AGL). The rest of the damage swath was located near an airport; therefore, the aerial survey could not be conducted. Aerial videos of 59 min in total length were obtained. Visual observations, including a number of urban traffic surveillance videos of strong winds, and publicly available photographs and videos of the condensation funnel provided by Youku.com, V.qq.com, and Weibo.com were collected. All of the information was checked for consistency and merged

to produce a comprehensive map of the damage swath that was overlaid on the satellite view imagery from Google Earth (Fig. 3), in which the high-resolution satellite images were taken on 24–25 August 2015. The analyzed tornado centerline was determined by the center of swath-scale convergent or rotational patterns of tree fall or debris, or the condensation funnel from the videos.

The locations and directions of fallen trees and transmission towers (or poles) were determined by

the ground survey at different places. Their locations were recorded by handheld GPS devices, and the directions of fallen structures were recorded by a compass and a camera. By comparing the locations of some isolated landmarks (e.g., trees) recorded by the GPS device to those on Google Earth, locating error in Google Earth was found to be generally within 10 m (mostly within 5 m). Most of this information was further checked with those obtained in the aerial videos, and then the directions of fallen structures

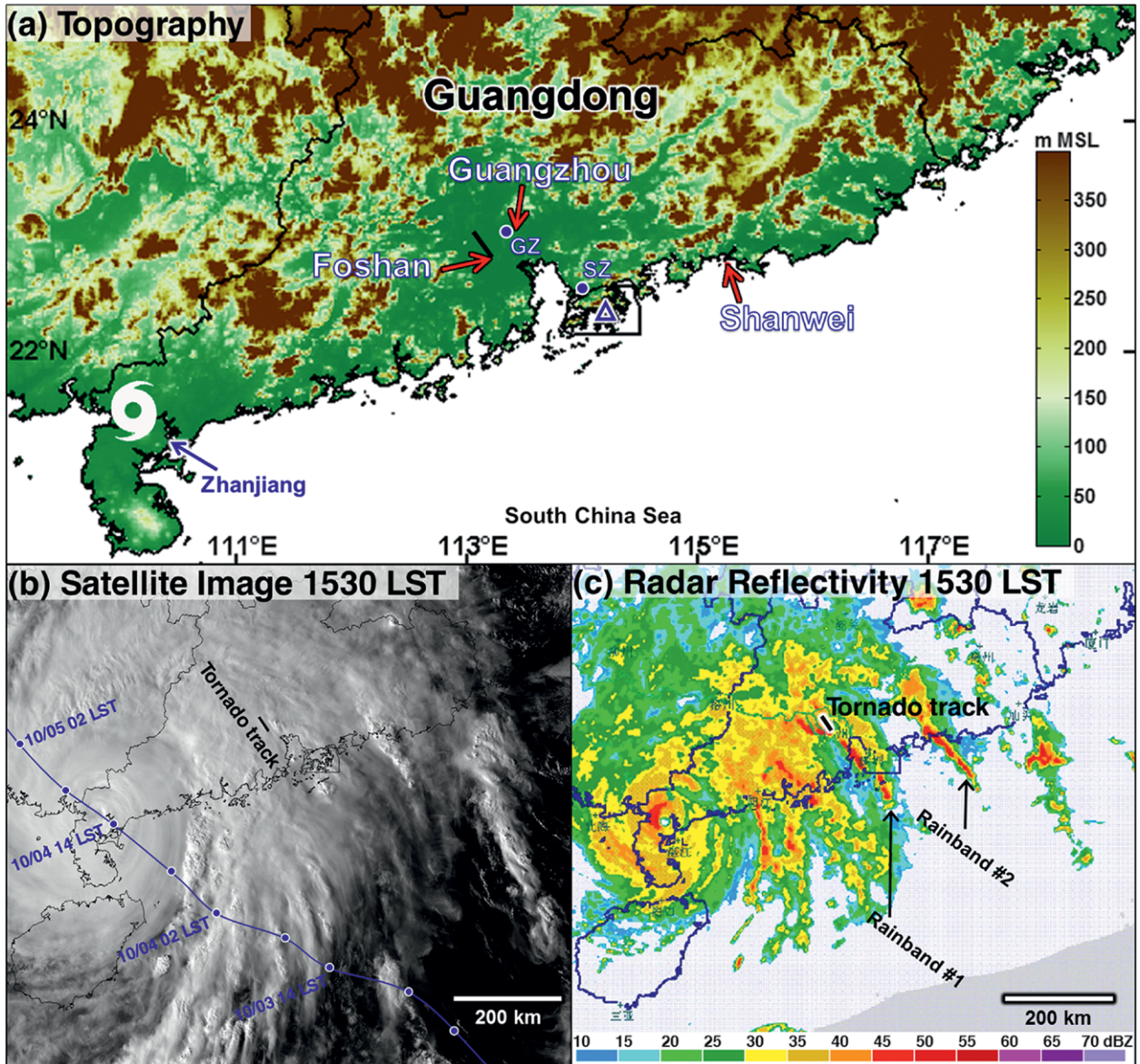


FIG. 1. (a) Terrain around Guangdong Province. The approximate location of the Foshan, Guangzhou, and Shanwei tornadoes (red arrows), the Foshan tornado track (black line), the locations of the GZ and SZ Doppler radars (blue dots), the eye of Typhoon Mujigae at 1530 LST 4 Oct 2015 (white typhoon symbol), and the location of the Hong Kong radiosonde (blue triangle) are shown. (b) Visible image at 1530 LST from *Himawari-8* with the Foshan tornado track (black line). Part of the typhoon track is shown (blue line). (c) Composite radar reflectivity at 1530 LST with the Foshan tornado track (thick black line).

obtained from the compass in the ground survey were translated onto the Google satellite view imagery in order to show the horizontal distribution of the near-surface wind pattern in a larger extent by looking downward from directly above.

The location of the tornado in the videos was geolocated on Google Earth by comparing the movement of the condensation funnel and the variation of debris in the videos with the tornado track, nearby landmarks, and their damage features obtained from both ground and aerial surveys. The horizontal distance from a camera to the tornado was then estimated based on Google Earth using its ruler tool. The uncertainty in the distance estimation was mainly from locating the condensation funnel at the ground. Farther spots from the camera would have greater location errors.

The damage to structures along the tornado track was rated using the EF scale (WSEC 2006) by the National Weather Service EFkit software (LaDue and Mahoney 2006). Although the degree of damage (DOD) identified for estimating wind speeds was

based on U.S. construction practices (WSEC 2006), the general similarity of the damage indicators (DIs) during this event to their U.S. counterparts gave us reasonable confidence to apply the EF scale to rate the intensity of the Foshan tornado.

The building codes and standards in China have been evolving in the past few decades, which were greatly influenced by Russia, Japan, Australia, the United Kingdom, Canada, and the United States (Tucker 2016). In China, the codes of tall buildings in large cities are similar to those in the United States, while differences mainly exist in small rural constructions. In Foshan, construction practices of one- and two-family residences in the rural area are generally similar to those in the United States [refer to the examples described in WSEC (2006)]. The walls of these residences mainly consist of veneer bricks covered (or not) by stucco (e.g., Fig. 4a), usually without reinforcement steel bars inside the frames. There are many light-frame steel constructions, enveloped by polyurethane composite panels, working as sheds built nearby fishponds in the rural area (e.g., Fig. 4b). These

small constructions were regarded as DI 3 (manufactured homes, single wide; WSEC 2006). There are many warehouses and industrial facilities in Foshan. Most of these constructions are metal building systems with single-bay rigid frames, Z- or C-shaped purlins, and girts that span between rigid frames. The frames of such buildings are usually made from galvanized steel and are enveloped by a standing seam roof but are not enclosed in the building envelopes (e.g., Figs. 4c,d). Most roof coverings are galvanized metal sheets with a thickness of 2–2.5 mm (often coated in blue; e.g., Fig. 4d), while exterior walls generally consist of laminboards with galvanized metal sheet outside and rockwool, glass fiber wool, or polyurethane foam insulation inside. These walls generally have a small percentage of window



FIG. 2. (a) Tornado track (black dashed line) with rated EF scales at some detailed ground survey sites (red dots) mapped onto the Google map. (b)–(j) On-site damage photographs at some locations along the tornado track. North is indicated by a white arrow in the upper-right corner.

FIG. 3. Damage map of the Foshan tornado on 4 Oct 2015 plotted on the Google Earth satellite view imagery. (left to right) Entire tornado damage path is divided into five parts. The bottom of the left panel is the beginning of the tornado path, and the top of the right panel is the end of the tornado path. As in Fig. 2, ground survey sites are indicated. Tornado translation direction (yellow arrow). Contours denote EF0 (white), EF1 (black), EF2 (green), and EF3 (red) damage intensity isopleths. Analyzed tornado centerline (yellow dashed line). (bottom right) North is indicated by a white arrow within the red shading.



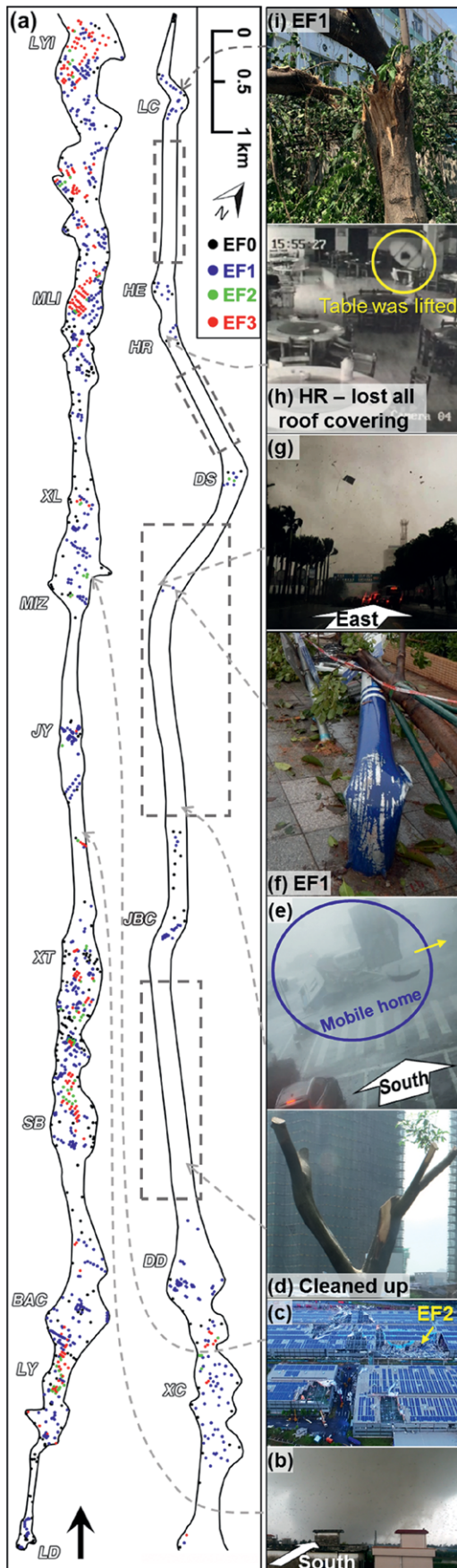
glass. These constructions are comparable to some metal building warehouses (refer to the examples of DI 21 in WSEC 2006) in the United States. There are also a few warehouses or industrial buildings whose frames and exterior walls are made by veneer bricks covered by stucco (e.g., Fig. 4e), or just the frames are made by reinforced concrete (e.g., Fig. 4f). These constructions were regarded as DI 23 (warehouse building; WSEC 2006).

In this study, we rated only those constructions that we thought were comparable to one of the 28 DIs listed in WSEC (2006). During the Foshan tornado event, the main damaged constructions were factories or warehouses that were built with steel structures and were quite similar to DI 21 in WSEC (2006) (e.g., Figs. 4c,d). We believe that the uncertainties associated with the reasonably small differences in construction codes between China and the United States can be taken into account by the EFkit software, which uses the expected value for wind speed estimation. Transmission poles or towers, and trees were reasonably treated as the same as their counterparts in the United States.

Based on both ground and aerial surveys, a total of 1,259 structures were rated



FIG. 4. Examples of artificial constructions in Foshan.



(their locations are given in Fig. 5a). In the first half of the damage swath, the uncertainty of the tornado intensity estimated by EF-scale damage ratings was mainly over farmlands and water areas because of the lack of DIs (e.g., fishponds and waterways; refer to the background images in Fig. 3). The narrow width of EF0 isopleths over some agricultural plots probably resulted from the same reason. In the latter part of the damage swath, which was located in the urban area, the majority of damaged structures were trees on streets. However, they were quickly cleaned up by the local government in some places (e.g., Fig. 5d); therefore, the damage indicators cannot be rated precisely. These damaged areas (denoted by dashed boxes in Fig. 5a) were conservatively rated EF0. Together with some visual evidence (e.g., Figs. 5e–i), the tornado track was ultimately determined.

Other observations. The Guangzhou (GZ) and Shenzhen (SZ) S-band Doppler radar (~24 km to the northeast and ~100 km to the southeast of the center of the tornado damage path; Fig. 1a) level-II data were used to analyze the parent weather systems of the tornado. These radars are similar to the Weather Surveillance Radar-1988 Doppler (WSR-88D) operating in the United States, in both their hardware and software (Zhu and Zhu 2004), operating in volume coverage pattern 21 (VCP21), scanning nine elevation angles of 0.5°, 1.5°, 2.4°, 3.4°, 4.3°, 6°, 9.9°, 14.6°, and 19.5° with a volumetric update time of 6 min during this event. The elevations of the radar antennas are 180.8 and 149.1 m above mean sea level (MSL) for the Guangzhou and Shenzhen radars, respectively. The three-dimensional analyses of the radar data were performed with the Gibson Ridge Level II Analyst radar-viewing software (www.grlevelx.com/).

Surface wind (2-min average) at a 5-min interval from a mesonetwork of in situ surface weather stations

FIG. 5. (a) Locations of all the rated structures with (b)–(i) some on-site damage photographs or video snapshots at some locations (indicated by dashed arrows). Denoted in (a) are the EF0 (black dots), EF1 (blue dots), EF2 (green dots), and EF3 (red dots) damaged structures. Entire tornado damage swath (denoted by the black EF0 contour) in (a) is divided into two parts. The left side of (a) indicates the first half of the damage path; the right side of (a) indicates the second half of the path. Tornado translation direction is indicated (black arrow) at the bottom of (a). Damaged areas in which the damaged structures had been quickly cleaned up by the local government are indicated (dashed boxes). Shown in (e) is a damaged mobile home on the street that was moving toward the west (yellow arrow).

(with a spatial resolution of about 4.5 km) from Foshan Meteorological Service, National Centers for Environmental Prediction (NCEP) Final Operational Global Analysis (NCEP FNL; $1^\circ \times 1^\circ$), visible satellite imagery, and conventional radiosondes were also used to examine the storm environment. The satellite data were from the new-generation geostationary meteorological satellite *Himawari-8* operated by the Meteorological Satellite Center of the Japan Meteorological Agency, with a time interval of 10 min and a resolution of 1 km at nadir.

DAMAGE SURVEY RESULTS. *Tornado track, attendant damage, and rating.* The tornado moved

along a line from the southeast near LD to the northwest near LC (Fig. 2). Detailed EF ratings were depicted on the high-resolution satellite view imagery from Google Earth (Fig. 3). The entire tornado damage swath was approximately 30.85 km long and 20–570 m wide. Probably because of the northwestward movement of the tornado overlapped with its system-relative cyclonic rotation, a larger area of damage was found on the right side of the tornado center than on the left side with respect to the tornado motion (Fig. 3).

The tornado began producing EF0 damage at ~1528 LST at LD as confirmed by the local residents. It then rapidly produced EF3 damage approximately

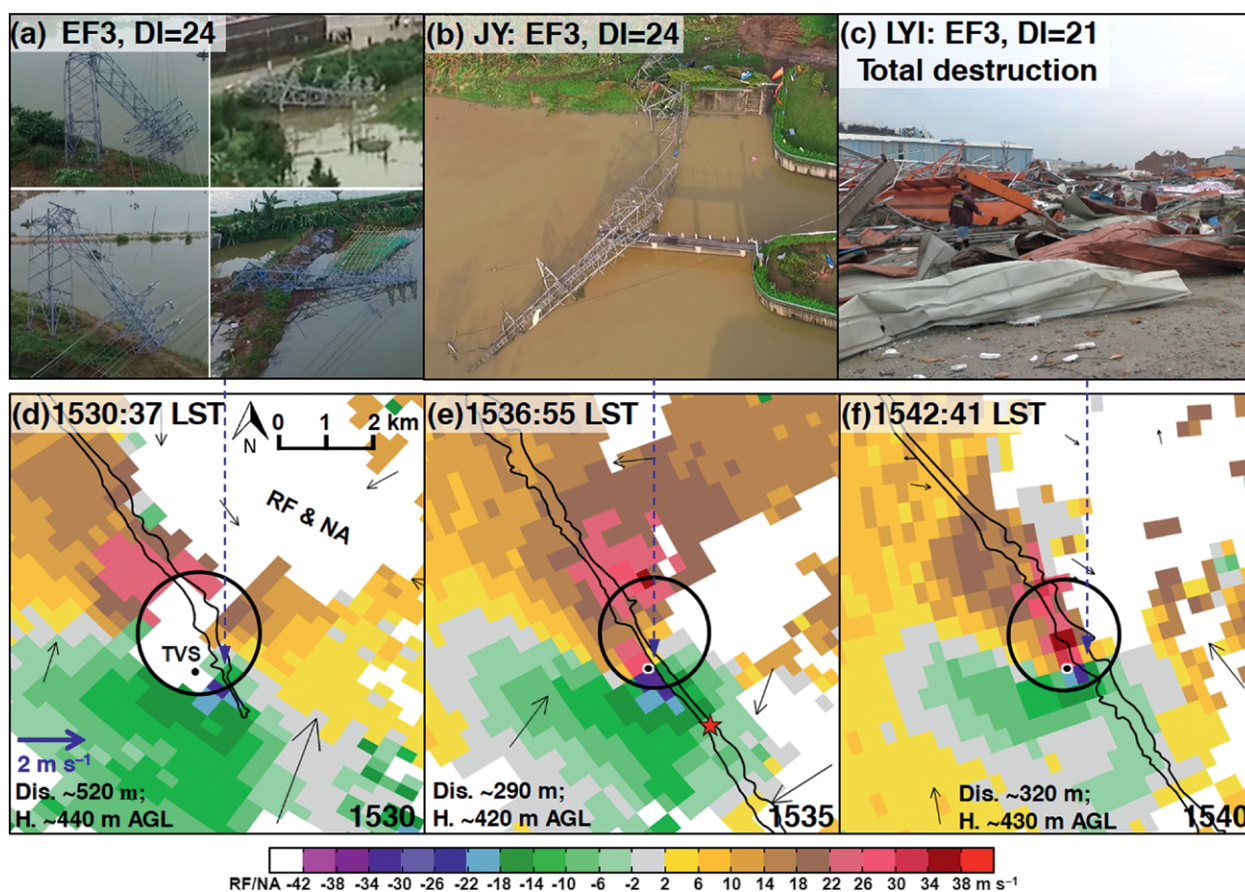


FIG. 6. (a)–(c) Images showing the most severe damage near the TVS locations [black dots in (d)–(f)]. (d)–(f) Radar radial velocity (shading, m s^{-1}). Locations of the damage structures in (a)–(c) are indicated (dashed blue arrows). The times in (d)–(f) are the recorded receiving time of the TVS radar beams. All radar data are from the 0.5° scans of the Guangzhou radar. Areas of range-folded or missing velocities (RF/NA) are shown (white shading). Across-track deviation (Dis) of the TVS location and the height (H) of the TVS are given at the bottom of each panel. Mesocyclones with the estimated diameter (black circles) and EF0 isopleth of the tornado (black contours) are indicated. Mesocyclone in (d) was estimated using the recognizable radial velocity pixels that satisfied the criterion, while the TVS location is roughly determined according to the morphology of the anomalously large radial velocity in the next volume scan [(e)]. The red star in (e) represents the estimated location of the tornado at 1536:55 LST. Vector difference of 10-m wind (black arrows) at the given time (LST; which is indicated by the number in the bottom-right corner in each panel) from that of 5 min before. Distance and vector length scales and north direction for (d)–(f) are given in (d).

3 min later near LY (e.g., four transmission towers were broken or collapsed; Figs. 2b, 6a). At ~1538 LST, a transmission tower was twisted and collapsed (rated EF3) on the south side of Shunde Waterway in JY (Figs. 2d, 6b). After the tornado produced EF2 damage in MIZ, it subsequently created EF3 damage in XL, where two metal truss tower cranes were broken (e.g., Fig. 2e). The most severe damage occurred in MLI and LYI, where the majority of constructions were metal building warehouses or factories and were roughly located in the middle of the tornado track (Figs. 2f,g, 3). A number of such DIs were totally destroyed (rated EF3; e.g., Fig. 6c). The damage swath was the widest (~570 m) in LYI (Fig. 3). Passing LYI, the tornado subsequently weakened while it moved northwest, passing by the urban area of Foshan; it stopped producing EF0 damage at about 1600 LST around LC (Figs. 2h–j, 3). Thus, the Foshan tornado had a life cycle of approximately 32 min.

Surface wind and tornado diameter estimation. The initial tornado wind field was estimated based on tornado videos, debris, and directions of fallen structures (e.g., trees and transmission poles or towers). Tornado videos showed that the surface wind was generally convergent outside the condensation funnel and cyclonic near the condensation funnel. However, the ground damage pattern revealed by tree falls could be either convergent or cyclonic near the condensation funnel, and is generally highly convergent outside the condensation funnel.

The most comprehensive information was collected from LY to BAC, where the tornado started to produce EF3 damage (Figs. 3, 7a). Videos of the condensation funnel taken at five spots approximately 200–2,000 m away from the tornado center were available, some of which made it possible to estimate the size of the condensation funnel and surface wind pattern. These camera locations were confirmed during the ground survey. The pond surface in this

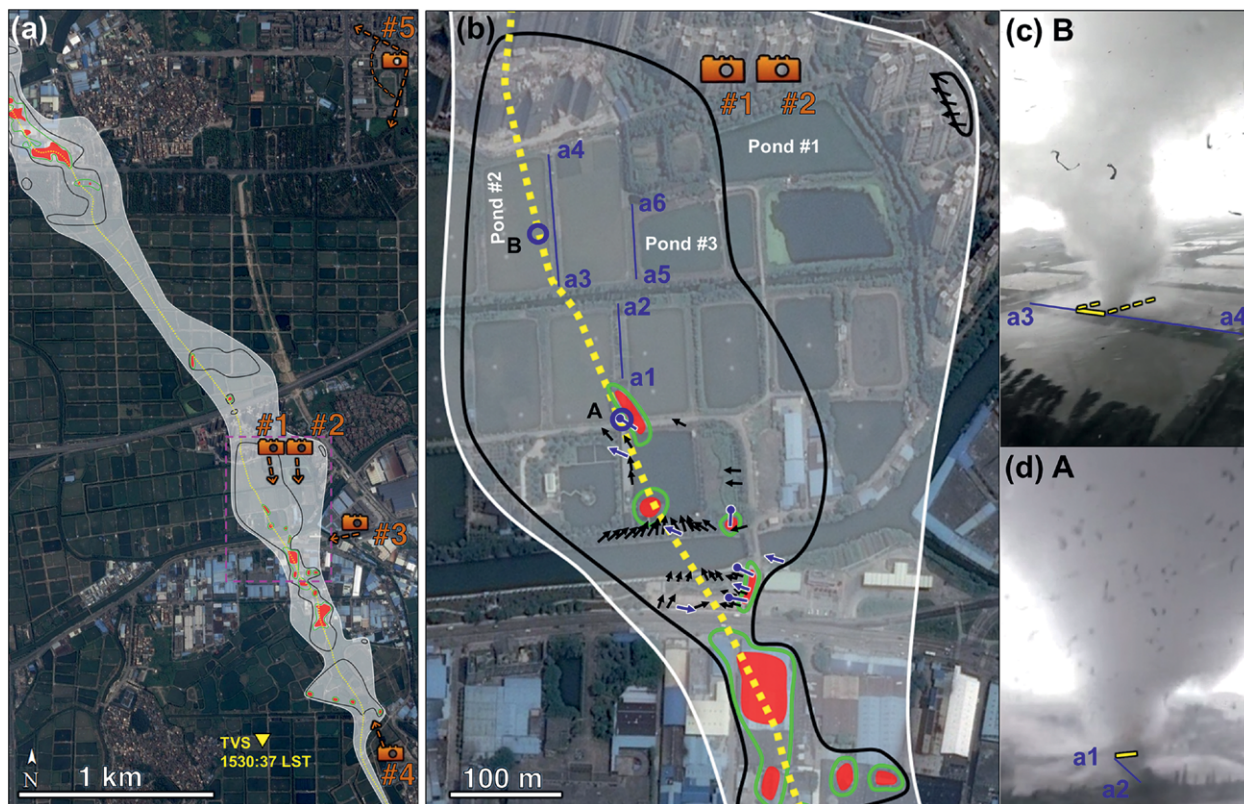


FIG. 7. (a) Detailed damage map at LY, BAC, and SB areas adapted from Fig. 3. Real-time video recording locations mentioned in the text (orange camera logos and corresponding numerical symbols) and directions to which the cameras are pointing (orange arrows) are shown. (b) Zoomed-in view of the magenta boxed area in (a). The size of the condensation funnels A and B (blue circles), directions of tree fall (black arrows), metal road signs (blue arrows), and transmission poles or towers (blue sticks with a rounded head) are all shown. (c),(d) Condensation funnel [corresponding to locations B and A in (b), respectively] snapshots from the video taken by camera 1. Lines a1–a2, a3–a4, and a5–a6 in (b)–(d) represent the roads close to the tornado.

area turned out to be quite useful for estimating the surface wind pattern by the movement of waves and sprays caused by the debris. Because the spray caused by the fallen debris has characteristics of low resistance and small mass (small inertia), it could be a good tracer for estimating the direction and speed of the near-surface flow around the tornado.

Variations of near-surface winds with the progressively decreasing of the distance of the tornado center to camera 2 (location is given in Fig. 7b) were obtained at BAC. The apparent wind started to blow over pond 1, which was close to camera 2 when the tornado was about 900 ± 50 m away from it, as reflected by the pond surface changing from calm to the appearance of waves propagating toward the tornado (Fig. 8a). Then, 11 s later, trees started to blow toward the tornado when the tornado was about 760 ± 50 m away (Fig. 8b); 3 s later, the debris flying around the tornado started to fall into pond 1 with the resulting sprays moving toward the tornado (Fig. 8c). When the tornado was about 350 ± 30 m away, debris close to the location of camera 2 was observed flying toward the tornado (Fig. 8d).

These features demonstrated an apparent convergent wind toward the tornado center at the location hundreds of meters ahead of the condensation funnel.

The pattern of near-surface winds of the tornado was clearly revealed by the movement of the sprays (Figs. 9a–c). Winds outside the condensation funnel were observed pointing straight toward the tornado, while apparent cyclonic circulation was indicated by the spray near the condensation funnel. Similar wind patterns were also observed by camera 3 (location is given in Fig. 7a), from a driver of a car 370 ± 30 m away from the tornado (Figs. 9d–f), in which a small sheet of material (denoted A) was blown away from the car toward the tornado while the debris at the edge of the condensation funnel was rotating cyclonically (denoted B, which is enlarged in the corresponding inset). These visual features clearly demonstrated convergent wind near the surface outside the condensation funnel and cyclonic wind near the condensation funnel both at the surface and aloft.

The abovementioned wind features shown by tornado videos were consistent with the wind

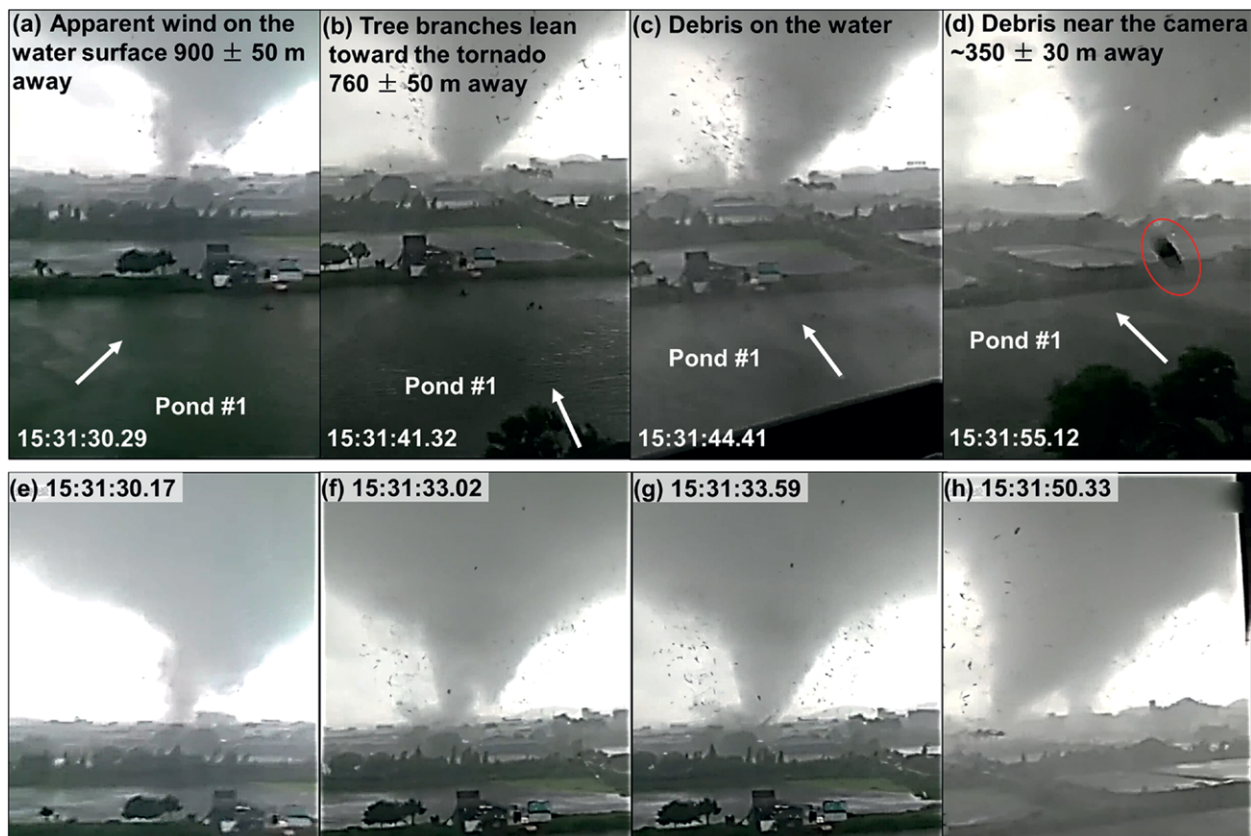


FIG. 8. Video frames from camera 2 (Fig. 7a) at different times (LST; hour:minute:second) showing (a)–(d) the wind features at different distances from the camera and (e)–(h) two occurrences of vertical subvortices. Wind direction mentioned in the text is shown in (a)–(d) (white arrows). In (d) a piece of debris (red circle) flying toward the tornado. Location of pond 1 in (a)–(d) is given in Fig. 7b. (This video was taken by Sheng Huang.)



FIG. 9. (a)–(c) Snapshots from the video taken by camera 1 in Fig. 7a. Direction of the motion of the spray caused by the fallen debris outside the condensation funnel (yellow arrows) and in (b) the direction of the motion of the condensation funnel (red arrow) are shown. (d)–(f) Snapshots from the video taken by camera 3 in Fig. 7a. In (d) and (e) debris rotating cyclonically at the edge of the condensation funnel (yellow circles) and each inset shows a zoomed-in view of the area around circle B. Direction of the movement of the condensation funnel (white arrow) is shown in (e). Time (minute:second) relative to the beginning of the given video is given in each panel.

patterns estimated by tree falls at JY and DD (Figs. 10a,e). An apparent cyclonic circulation (with a diameter of ~30 m) was observed near the centerline of the damage swath, while an apparent convergent wind pattern was observed farther away from the swath centerline. The eastward wind on the left side of the tornado center, indicated by both the tree falls (Fig. 10a) and visual observations from camera 6 (Fig. 10c location is given in Fig. 10a), converged with the westward wind from the rotating circulation, producing a highly convergent zone on the left side of the tornado center (Fig. 10a). The ground-survey-based wind pattern agreed well with that from the aerial survey (Fig. 10b). This wind pattern was quite similar to what was observed in Atkins et al. (2014) about the Moore,

Oklahoma, EF5 tornado in 2013. They found that a cyclonic pattern of fallen trees was mainly located within the condensation funnel and embedded within EF2, EF3, and EF4 isopleths, and that the diameter

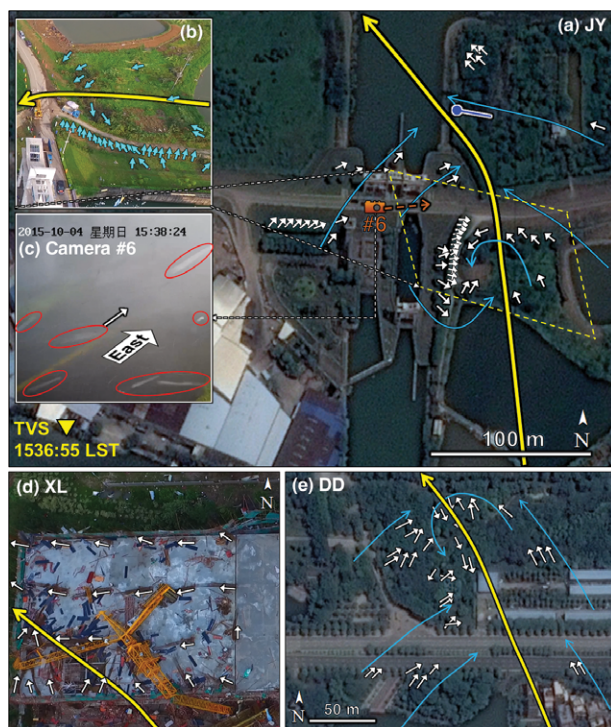


FIG. 10. (a) Directions of fallen trees (white arrows) and a transmission tower (blue stick with a round head) marked on the Google Earth satellite view imagery at JY. The blue arrows denote the estimated initial tornado wind field. Traffic surveillance camera 6 (orange camera logo) and direction in which the camera is pointing (dashed orange arrow) are shown. TVS location at 1536:55 LST is denoted by the yellow triangle in the lower-left corner. (b) Aerial photograph of the area in the dashed yellow box in (a) with the light blue arrows denoting the tree fall. (c) Snapshot of camera 6, in which the near-surface debris (red circles) was moving toward the east (thin white arrow). (d) Snapshot from the video taken by the drone with the direction of bend of metal trusses (white arrows) marked on the top of a building under construction at XL. (e) As in (a), but at DD. Analyzed tornado centerline (yellow arrow) are shown in each panel.

of the cyclonic pattern was much smaller than the condensation funnel size. However, at some other places, instead of cyclonic rotation, convergent winds were indicated all the way down to the tornado center. For example, the fallen trees to the south of location A in Fig. 7b demonstrated a highly convergent wind pattern. The bent rebar on the top of a building under construction (~12 m AGL) at XL also demonstrated apparent convergent winds near the tornado center (Fig. 10d).

Surface wind speed of the tornado to the south of BAC (near pond 3 in Fig. 7b) was estimated based on the movement of the spray raised by the debris of the tornado when the tornado was within 300 m of camera 1 (Figs. 9a–c) and was compared to EF-scale estimation. By checking the video of camera 1 frame by frame [frame rate = 29.914 frames per second (fps)], the west edge of the spray (indicated by the yellow arrow in Fig. 11a) caused by a piece of debris that fell into pond 3 was observed close to the land–water boundary in frame 0. Then 12 frames later, the spray moved across the road a5–a6 to be right over the land–water boundary on the other side of the road (Fig. 11b). The derived wind speed of the near-surface flow was at least $32.2 \pm 2.9 \text{ m s}^{-1}$. The uncertainty was mainly from the time interval between two continuous video frames. The speed of the near-surface wind here estimated based on the visual observation was comparable to that estimated in EF scale. About 25 m south of this location, one banana tree located close to water was uprooted (Fig. 11c) and a large branch of a neighboring pine (softwood; DI 28) was broken. According to the EFkit, the expected value of the assigned DOD was 33.5 m s^{-1} , rated EF0 ($29\text{--}38 \text{ m s}^{-1}$), which was quite close to the visually estimated wind speed of $32.2 \pm 2.9 \text{ m s}^{-1}$.

The diameter of the condensation funnel at the ground at spot B to the south of BAC (Figs. 7b,c) was estimated by superposing translucently the video frame on the on-site photograph in Photoshop software (Figs. 12a,b). The on-site photograph was then stretched to guarantee the boundaries of the fishponds around the condensation funnel were completely matched with those in the video frame. The two ends of the diameter of the condensation

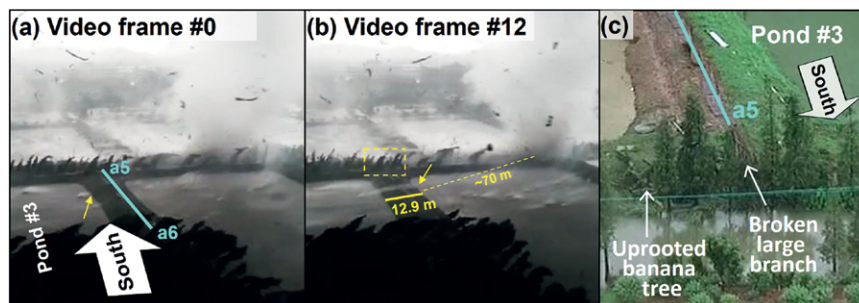


FIG. 11. (a),(b) Video frames from camera 1 in Fig. 7a. Video frame in (b) is the 12th frame after that in (a). In (a) and (b) the west edge of the spray (yellow arrows) caused by the debris that fell into pond 3 (location is given in Fig. 7b) is shown. In (b) width of land–water boundaries (solid yellow line), and rough distance from the spray in question to the tornado center (dashed yellow line). (c) Aerial video snapshot showing the tree damage indicators within the yellow box denoted in (b). Road a5–a6 denoted in Fig. 7b is shown (cyan line).

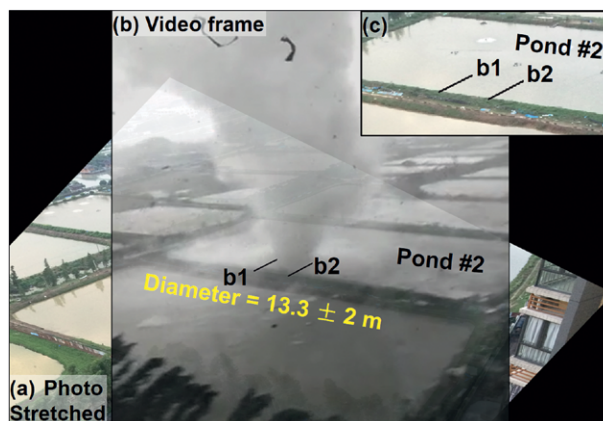


FIG. 12. (a) On-site photograph overlaid with (b) a video snapshot of camera 1 (location is given in Fig. 7b). Video frame was adjusted translucently to match the landmarks in (a) using Photoshop software. Location of pond 2 is given in Fig. 7b. Two ends (black lines b1 and b2) of the diameter of the condensation funnel at the ground are marked on (c) the enlarged on-site photograph.

funnel at the ground were then marked on the on-site photograph (b1 and b2, respectively, in Figs. 12b,c), and the diameter of the condensation funnel was finally obtained (13.3 m with an error of $\pm 2 \text{ m}$) by measuring the horizontal distance on-site between these two marks using a tape. The diameter of the condensation funnel at spot A (Figs. 7b,d) was obtained in the same way, which was $15.7 \pm 4 \text{ m}$. The diameter of the condensation funnel at the ground was generally smaller than the extent of the EF2 isopleths (Fig. 7b).

Some visual features of the tornado. The video taken by camera 2 at BAC showed two occurrences of

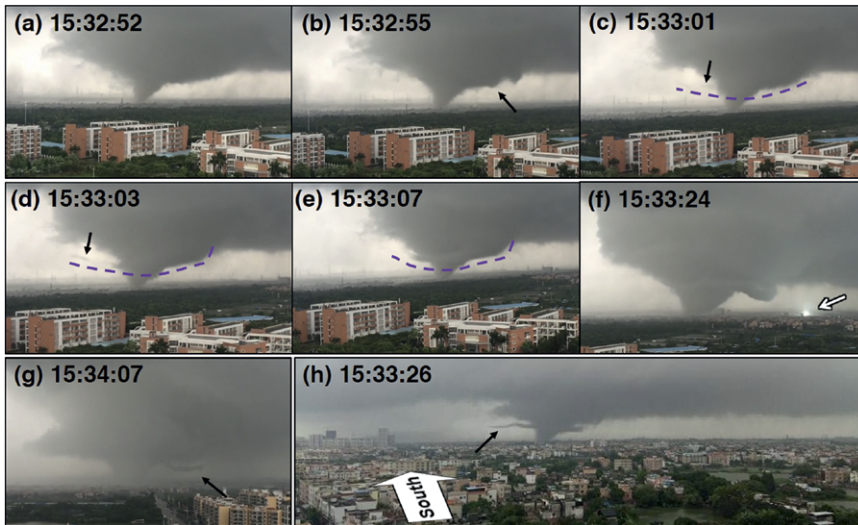


FIG. 13. Evolution of the horizontal condensation tube. (a)–(g) Snapshots from the video taken by camera 5 in Fig. 7a at different times (LST; hour:minute:second). Horizontal condensation tube (dashed purple line and black arrow) is indicated. The white arrow in (f) indicates the power flash at the ground. (h) Photo provided by Kangdong Lin taken about 2.5 km to the north of camera 5.

subvortices within a 20-s period (Figs. 8e–h). At both times, the subvortices rotated with the original vortex after their formation and quickly merged with the primary tornado vortex within 2–3 s. The formation of the subvortex happened when the tornado passed a building with the sudden increase of debris.

A visually observed horizontal condensation tube formed on the rear-flank side beneath the cloud base near the tornado condensation funnel about 90 s after the merging of the second subvortex, as shown in a video recorded by camera

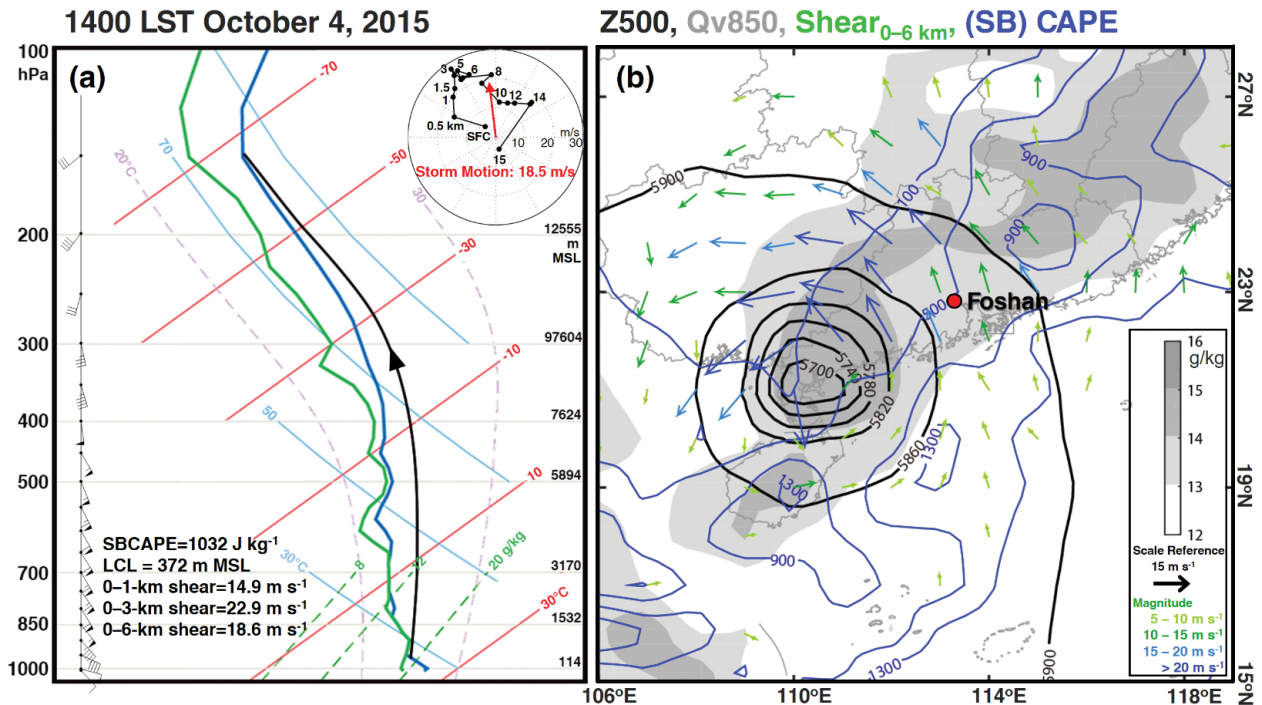


FIG. 14. (a) Skew T - $\log p$ diagram showing the radiosonde observation in Hong Kong, China, at 1400 LST 4 Oct 2015. The path of the surface-based parcel is shown by the thick black line. The hodograph diagram is plotted in the upper-right corner and shows the storm-motion vector (red arrow). Numbers along the lines in the hodograph denote the altitude above the ground (km). Also shown on the left side of (a) are the horizontal wind bars at some levels (half barb = 2 m s⁻¹, full barb = 4 m s⁻¹, and pennant = 20 m s⁻¹). (b) Geopotential height at 500 hPa (black contours; gpm), water vapor mixing ratio at 850 hPa (shading; g kg⁻¹), surface-based CAPE (blue contours; J kg⁻¹), and 0–6-km vertical wind shear [vectors; the scale reference and magnitudes (reflected by different colors) of the vectors are shown in the bottom-right corner; m s⁻¹] at 1400 LST 4 Oct 2015 based on NCEP FNL. The location of Foshan is denoted by the red dot.

5 (location is given in Fig. 7a) (Fig. 13). This condensation tube formed during the intensifying stage of the tornado (1530–1536 LST), wrapped around the tornado with a long tail, and elongated with time. It lasted at least 90 s and vanished before the tornado arrived at JY (e.g., Fig. 5b). Following its formation, the horizontal condensation tube experienced a slightly downward motion and soon after a power flash at the ground was observed (the flare in Fig. 13f) close to this tube. Viewed from its tail, the horizontal vortex was rotating clockwise, which was the same direction as the horizontal vortex observed in the 24 May 2011 El Reno, Oklahoma, tornado (Bluestein et al. 2012; Houser et al. 2016). In that tornado, the horizontal vortex also formed as the tornado intensified (Houser et al. 2016) and then experienced a downward motion (Bluestein et al. 2012). Horizontal condensation tubes have been observed adjacent to many other violent midlatitude tornadoes, such as the 27 April 2011 Tuscaloosa, Alabama, tornado (Knupp et al. 2014) and the 14 April 2012 Langley, Kansas, tornado (Orf et al. 2017). Houser et al. (2016) found that there was a close relationship between the horizontal vortex and a secondary rear-flank gust front surge. In a finescale radar display, such a horizontal vortex was found accompanying a narrow band of cyclonically curved low reflectivity and a convergent pattern of radial velocity (Bluestein et al. 2012; Houser et al. 2016). Such finescale features, however, were not captured in the Foshan case probably because the tornado was not quite close to (~24 km away) the Guangzhou radar.

ENVIRONMENTAL FEATURES. TC environment.

When Typhoon Mujigae made landfall around 1.5 h before the genesis of the Foshan tornado, it was quite strong with the maximum wind speed of greater than 50 m s^{-1} (Zhao et al. 2017), which was favorable for tornadogenesis according to McCaul (1991; showing a mean intensity of 47.1 m s^{-1} for hurricanes

that produced more than eight tornadoes). Located ~350 km northeast of the TC center, the Foshan tornado was spawned in an environment characterized by moderate convective available potential energy (CAPE), low convective inhibition (CIN) (Figs. 14, 15a), rich low-level moisture (Fig. 14), and a 0–1-km vertical wind shear of 14.9 m s^{-1} (Figs. 14a, 15b). Probably because of the decrease of near-surface wind speed as

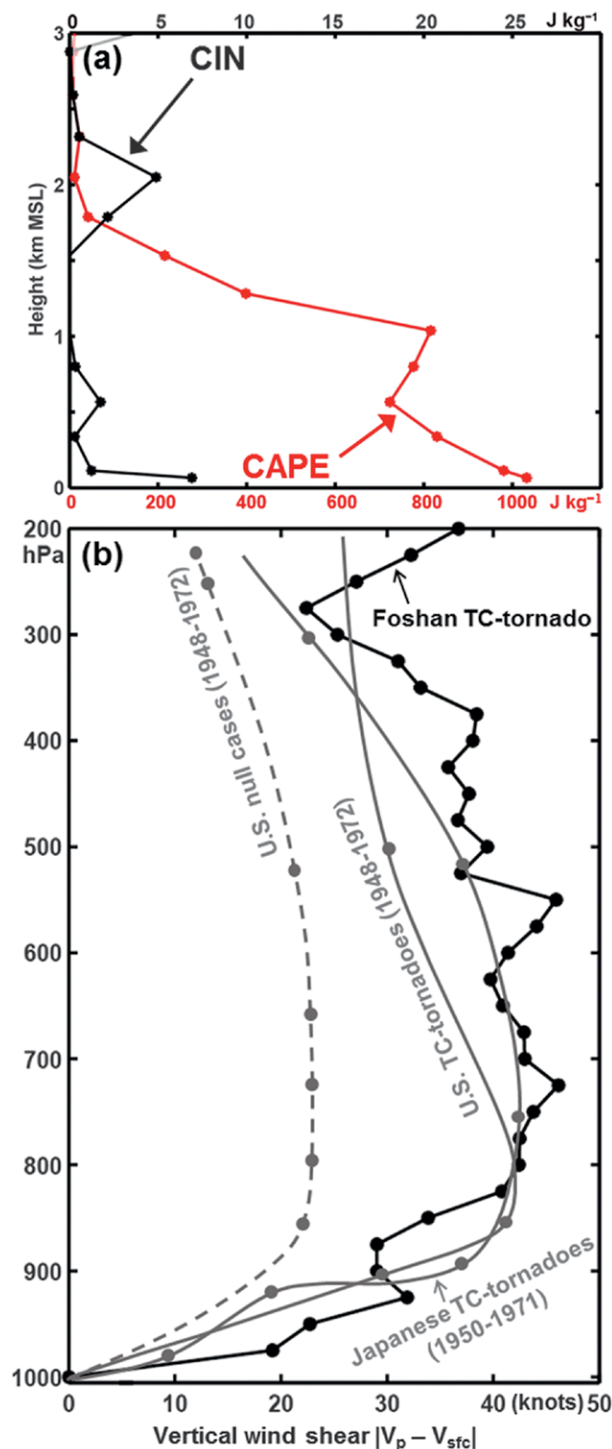


FIG. 15. (a) Vertical profiles of low-level CAPE (red) and CIN (black) (J kg^{-1}). (b) Vertical wind shear (kt; $1 \text{ kt} = 0.51 \text{ m s}^{-1}$) profile for the Foshan TC tornado (black curve) derived from the Hong Kong radiosonde observation in Fig. 14a. Sounding-derived proximity vertical wind shear (kt) profiles for TC tornadoes in Japan and the United States (solid gray curves) and right-front quadrant wind shears for U.S. hurricanes without tornadoes (dashed curve), which were adapted from Novlan and Gray (1974) are also plotted for comparison. Magnitude of the vertical wind shear was calculated between the winds at a given pressure level and the surface level.

a result of the increase of friction, the 0–6-km vertical wind shear increased from the sea toward inland in the northeast quadrant of the typhoon center (Fig. 14b).

The environmental parameters derived from the Hong Kong radiosonde [Fig. 14a; located ~114 km southeast of the tornado (Fig. 1a)] at 1400 LST 4 October 2015 were compared to both the radiosonde- and model-based U.S. climatology of TC tornadoes. In comparison to the TC tornado proximity sounding climatology summarized by Schneider and Sharp (2007), the sounding-derived environmental parameters in the Foshan case mainly fell in the high-tornado-threat category (Fig. 16a). The Foshan tornado occurred in the right-rear quadrant (111°) of the TC environment with respect to the TC motion. The most unstable CAPE at the lowest 3 km was equal to the surface-based CAPE with a magnitude of 1,032 J kg⁻¹ (Fig. 15a), which was comparable to the average CAPE of 1,031 J kg⁻¹ in the right-rear quadrant in the U.S. climatology of TC tornadoes (McCaul 1991) but much larger than the average CAPE (253 J kg⁻¹) regardless of the quadrant location (McCaul 1991). The vertical wind shear profile between a given pressure level and the surface showed identical characteristics to the Japanese TC tornadic environment climatology, which was comparable to the U.S. climatology below approximately 800 hPa but greater above (Fig. 15b).

The environment of the Foshan tornado was also compared to the supercellular TC tornado environment during 2003–11, obtained by blending the objectively analyzed surface observations with the Rapid Update Cycle model-analysis fields (Fig. 16b) (Edwards et al. 2012). Considering the composite parameters, the fixed-layer significant tornado parameter (STP; Thompson et al. 2003) of the Foshan tornado was distinctly greater than those in the United States and the supercell composite parameter (SCP; effective layer base) was located near the 75th percentile. The conditional instability was also located in the high category with the lowest 100-hPa mean mixed-layer (ML) CAPE (MLCAPE) located near the 75th percentile with apparently high precipitable water (PW). On the other hand, the vertical wind shear of the Foshan tornado case was not quite high. The 0–1-km storm relative helicity (SRH; 266 m⁻² s⁻²) was close to the median of the U.S. climatology, while the 0–6-km bulk wind difference (BWD; 18.6 m s⁻¹) was even near the lower bound of the 25th percentile for EF2 and EF3 TC tornadoes.

The parent supercell. Typhoon Mujigae produced at least five minisupercells in Guangdong Province,

and the supercells that spawned the Foshan and Guangzhou tornadoes were embedded in rainband 1, while the Shanwei waterspout was embedded in rainband 2, which was about 200 km farther away from the TC center (Fig. 1c). The rainbands that produced tornadoes were well organized in a narrowband shape and convectively active (e.g., Fig. 17a). Gaps between convective cells within these rainbands gradually increased as the cells approached the land. The convective cell that generated the Foshan tornado was initiated near the seashore, then intensified (in terms of composite radar reflectivity) immediately after it moved over land near Macau at 1418 LST, and then moved to the northwest along the rainband. A large gap sustained between this cell and its neighboring cell to the southeast until the dissipation of the tornado. This cell eventually developed into a supercell at around 1442 LST, when a mesocyclone was first identified. Details of the mesocyclone will be presented in the next section.

The Foshan supercell had a well-organized hook echo (Figs. 17b–g). The tornado damage swath was located near the tip of the hook echo. Anomalous large reflectivity (greater than 64.5 dBZ) at the 0.5° elevation angle was observed almost right over the tornado track at 1536 and 1542 LST (Figs. 17f,g). The hook echo was most probably caused by the debris raised from the ground, since the maximum reflectivity occurred at the lowest level and decreased with height (not shown; Bodine et al. 2013).

The Foshan tornadic minisupercell was characterized by a low radar echo top, which was similar to the minisupercells that were observed in TC environments in the United States (e.g., Spratt et al. 1997; McCaul et al. 2004). The radar echo top, which was defined here as the maximum height of 15-dBZ isosurfaces, remained at about 10 km AGL during the entire life cycle of the supercell except for at around 1450 LST, when the radar echo top reached approximately 12.3 km AGL with an overshooting cloud top first clearly detected in high-resolution satellite images. The overshooting cloud top started to be ripped apart from its lower part at ~1500 LST and drifted about 60° to the right of the tornado track (Fig. 18). One interesting feature that has been seldom observed in midlatitude supercells was that the overshooting cloud top of this TC tornadic supercell remained active despite having been ripped apart from the lower part; this feature awaits further investigation.

RADAR TORNADIC SIGNATURES.
Mesocyclone. A mesocyclone is a storm-scale (2–10 km in diameter) cyclonically rotating vortex,

usually with a vertical vorticity on the order of 10^{-2} s^{-1} or greater (American Meteorological Society 2016a). In addition to the criteria on vorticity and diameter, the detection of mesocyclones from Doppler radars usually includes two other criteria for traditional tornadoes: 1) a vertical extent of the rotational signature of at least 3 km and 2) the existence of the previous condition for at least 10 min (e.g., Spratt et al. 1997). In this study, a radar-derived mesocyclone was identified when a couplet of storm-relative inbound (V_{SRVin}) and outbound (V_{SRVout}) radial velocity maxima was detected to have a horizontal distance (diameter) of 1.5–10 km between each other with a rotational shear vorticity (McCaul

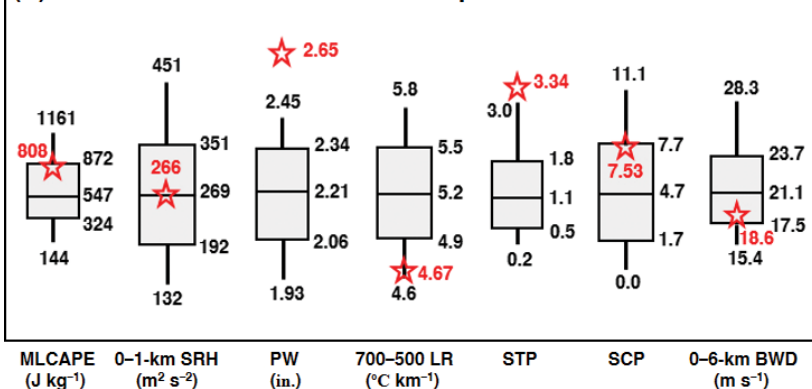
et al. 2004) greater than 0.01 s^{-1} in a vertical extent of 2 km, considering the typically shallower depths of TC tornadic mesocyclones compared to the traditional tornadic ones, and lasted at least 10 min. A diameter of 1.5–10 km instead of 2–10 km was used to make our results more comparable to other works (e.g., Spratt et al. 1997; Suzuki et al. 2000). The storm motion (18.1 m s^{-1} , 146.7°) was estimated based on the movement of the velocity-couplet signature detected by the Guangzhou radar.

The mesocyclone was first detected at 1442 LST with a vertical extent of approximately 2 km from 2 to 4 km AGL (Fig. 19a), lasting about 80 min. The maximum depth of the mesocyclone was mainly around

(a) Parameters in Foshan TC environment versus high TC-tornado threat

	Foshan TC-tornado	High threat
Location with respect to TC's motion direction	111°	$0^\circ\text{--}120^\circ$
Lifted index (surface-based parcel)	-3.5	< -2
CAPE (surface-based parcel)	1032 J kg^{-1}	$>500 \text{ J kg}^{-1}$
0–3-km shear	22.9 m s^{-1}	$>20 \text{ m s}^{-1}$
0–1-km storm relative helicity	$266 \text{ m}^2 \text{ s}^{-2}$	$>100 \text{ m}^2 \text{ s}^{-2}$
Bulk Richardson number	14.2	10–50
850-hPa wind speed	21.6 m s^{-1}	$>15 \text{ m s}^{-1}$
Storm motion (sounding derived)	18.5 m s^{-1}	$4\text{--}13 \text{ m s}^{-1}$

(b) Environment for TC tornadic supercell



(c) 0.5° peak V_{rot} (m s^{-1})

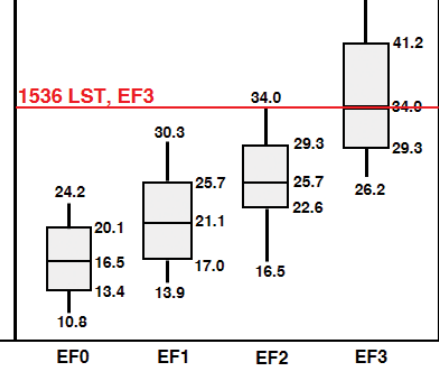


FIG. 16. (a) Parameters used to distinguish a low-threat and high-threat TC environment for tornadoes, which were adapted from McCaul (1991) and Schneider and Sharp (2007). These parameters for the Foshan TC tornado were calculated using the radiosonde observation in Fig. 14a. (b) Comparison of the parameters of the Foshan tornadic environment (red stars) calculated with the radiosonde observation in Fig. 14a to the U.S. climatology for supercellular TC tornado environment given by Edwards et al. (2012) (box-and-whisker plot; adapted from their Figs. 7c and 8). Parameters include MLCAPE (J kg^{-1}), 0–1-km AGL SRH ($\text{m}^2 \text{ s}^{-2}$), precipitable water (inches; 1 in. = 2.54 cm), 700–500-hPa lapse rate ($^\circ\text{C km}^{-1}$), STP (fixed layer), SCP (effective layer), and 0–6-km AGL BWD (box-and-whisker plot for EF2–EF3 TC tornadoes). (c) Box-and-whisker plot for 0.5° peak rotational velocity (V_{rot} , m s^{-1}) of EF0–EF3 tornado events reported in the contiguous United States during 2009–13 at 100–2,900 feet (1 ft \approx 0.305 m) above radar level, which were adapted from Smith et al. (2015). The 0.5° peak V_{rot} of the Foshan tornado event at 1536 LST (red line) were plotted onto the box-and-whisker diagrams for comparison. In (b) and (c), the percentile extents and corresponding values represent the 25th–75th percentiles for boxes, the 10th–90th percentiles for whisker, and the 50th percentile for lines in the boxes.

3 km AGL during the tornado life cycle, which was consistent with other tornadic minisupercells in TC rainbands (e.g., Spratt et al. 1997). The mesocyclone diameter ranged from 1.5 to 6.1 km at all elevation angles (Fig. 19b). It experienced a sharp decrease

near the tornado touchdown time (1520–1530 LST), which was similar to the diameter trend observed in minisupercells in the United States (e.g., Grant and Prentice 1996; Spratt et al. 1997). In the volume scan at around 1536 LST, the diameter at the lowest

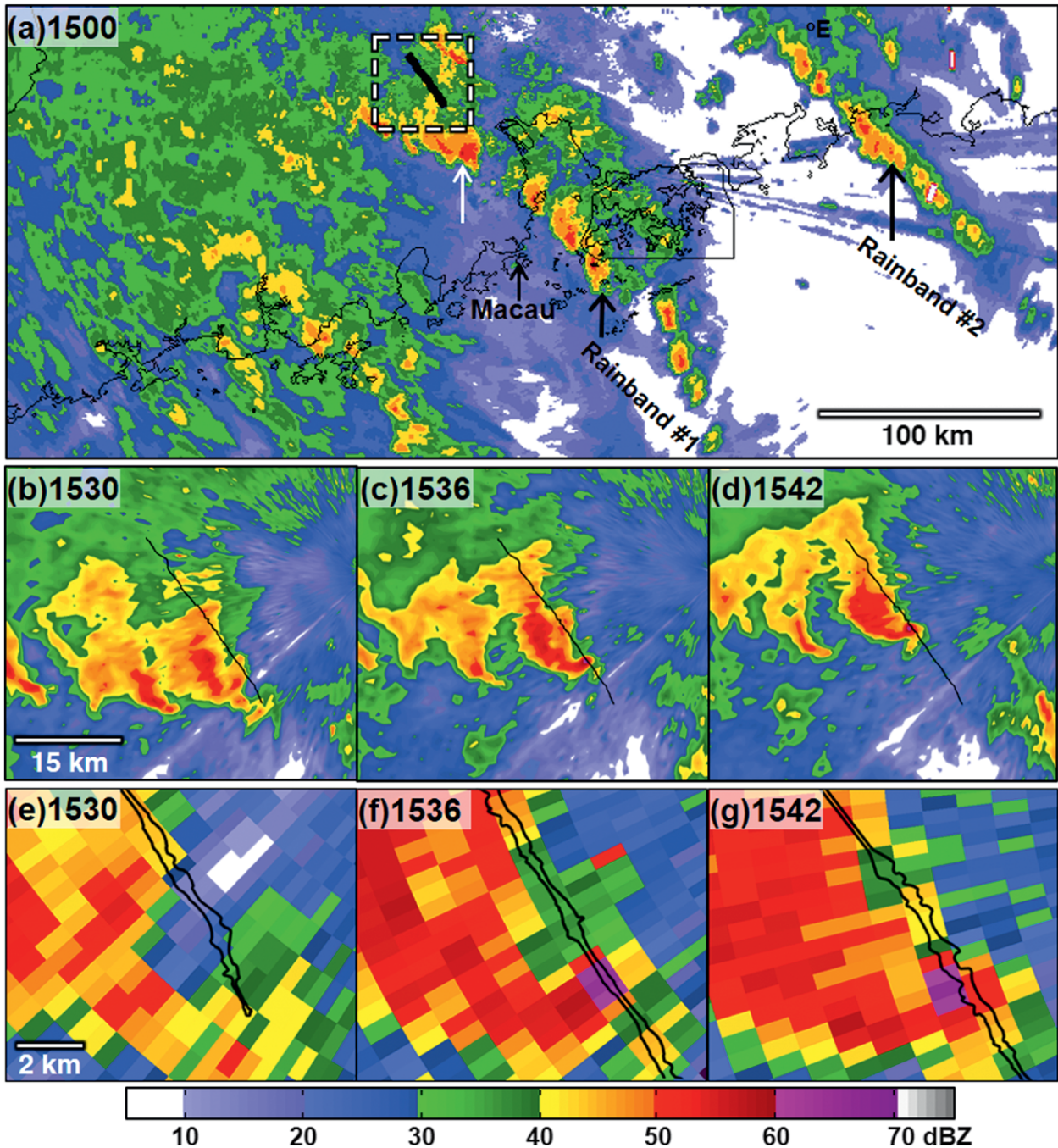


FIG. 17. (a) Composite radar reflectivity (shading, dBZ) at 1500 LST 4 Oct 2015. The white arrow indicates the Foshan tornadic supercell. Base reflectivity (shading, dBZ) at the 0.5° elevation angle in the dashed box in (a) are given at (b) 1530, (c) 1536, and (d) 1542 LST. The black line in (b)–(d) represents the Foshan tornado track. (e)–(g) Base reflectivity at the 0.5° elevation angle enlarged around the hook echo with EF0 isopleth (black) at (e) 1530, (f) 1536, and (g) 1542 LST. Distance scale for each row is given in (a), (b), and (e). All the base reflectivity data were from the Guangzhou radar.

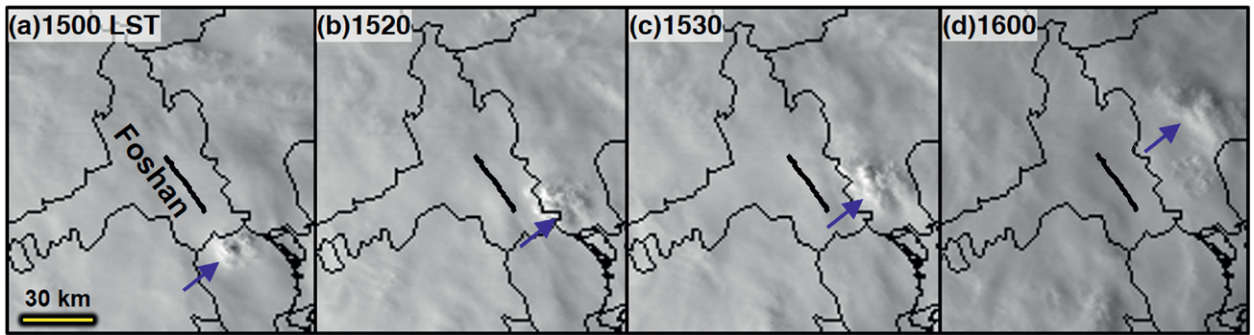


FIG. 18. Visible satellite images from *Himawari-8* at (a) 1500, (b) 1520, (c) 1530, and (d) 1600 LST 4 Oct 2015. Overshooting cloud top (blue arrows) of the parent supercell of the Foshan tornado and Foshan tornado track (thick black lines) are shown. Distance scale is given in (a).

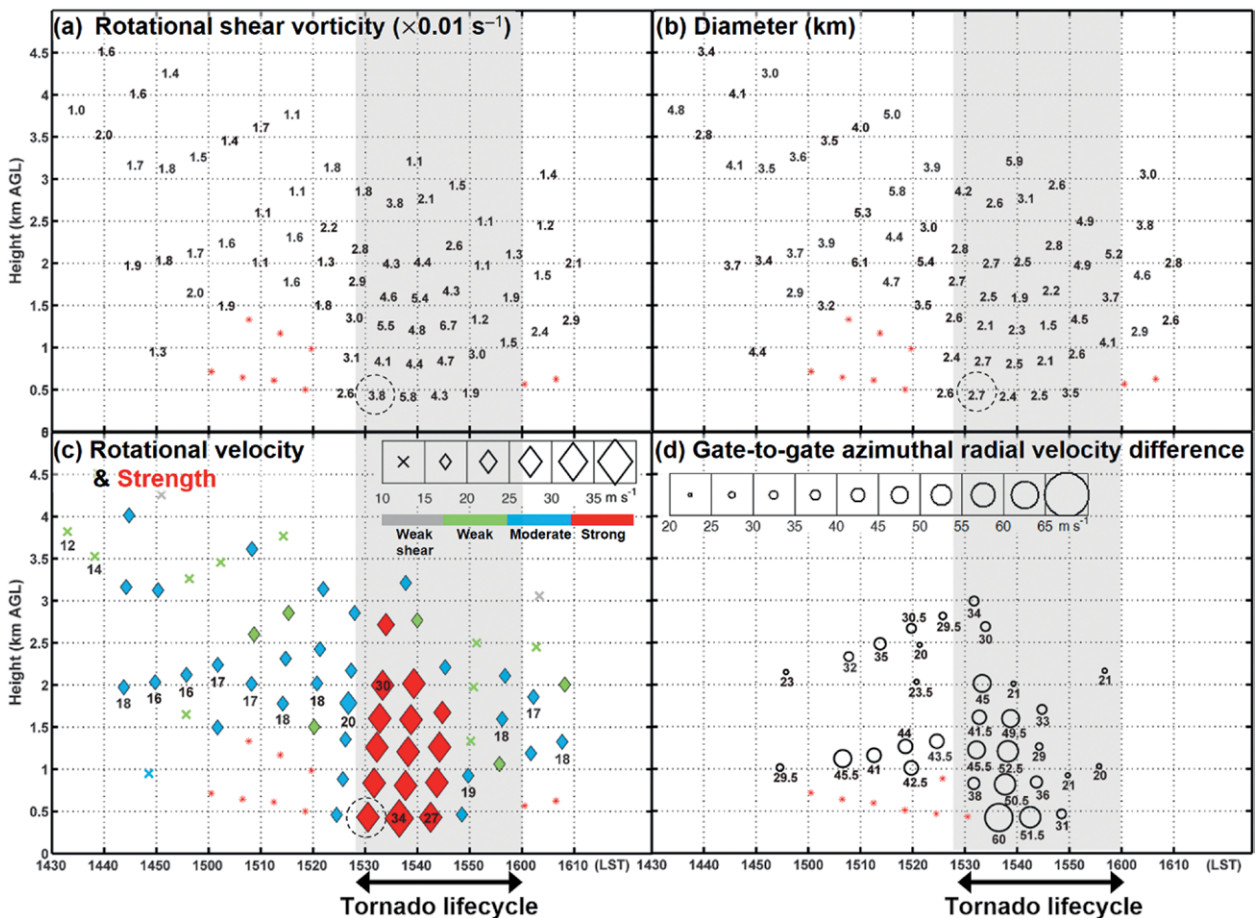


FIG. 19. Time–height diagrams of (a) rotational shear vorticity ($\times 0.01 \text{ s}^{-1}$), (b) diameter (km), (c) storm-relative rotational velocity (m s^{-1}) of the 2D velocity-couplet signature of the Foshan tornadic mesocyclone, and (d) maximum gate-to-gate azimuthal DV (over an azimuthal distance of one beamwidth) greater than 20 m s^{-1} within the mesocyclone. All the features were identified from the Guangzhou and Shenzhen Doppler radars. In (c), the maximum values of storm-relative rotational velocity within a volume scan time are labeled by numbers, and the strength of rotation (color shading) is categorized using the Radar Operations Center mesocyclone strength nomogram that assumes a diameter of 1.85 km for TC rainband mesocyclones adapted from Spratt et al. (1997; their Fig. 2b). Heights where the (a)–(c) mesocyclone and (d) DV were undetectable (red asterisk) because of the range-folded value are indicated. Values in dashed circles in (a)–(c) were derived using the recognizable radial velocity pixels where there were data dropouts as shown in Fig. 6d. Tornado life cycle is shaded in gray and denoted by the two-way arrow at the bottom for reference.

level contracted to about 2.4 km. The intensity of the mesocyclone peaked in this volume scan with the maximum rotational velocity [$V_R = (|V_{SRV_{in}}| + |V_{SRV_{out}}|)/2$] of 34 m s^{-1} (Fig. 19c) and the rotational shear vorticity (twice V_R divided by half the diameter; McCaul et al. 2004) of 0.058 s^{-1} (Fig. 19a) obtained at the lowest level. The maximum 0.5° peak rotational velocity in this EF3 Foshan tornado was close to the median of rotational velocities associated with EF3 tornadoes in the United States (Smith et al. 2015, their Fig. 5) (Fig. 16c). At this time, the areas JY, MIZ, and XL were located inside the mesocyclone at the 0.5° elevation angle (Figs. 6e,b). The most severe surface damage happened ~ 4 min later when the tornado hit MLI and the 0.5° mesocyclone was already in the weakening stage (Figs. 19a,c).

The strength of the Foshan tornadic mesocyclone below 2 km AGL was in the strong category (Fig. 19c) when the tornado was producing EF3 damage, according to the adjusted Radar Operations Center (previously the Operational Support Facility) mesocyclone strength nomogram for a diameter of 1.85 km, suggested by Spratt et al. (1997). The maximum mesocyclone azimuthal shear [$(|V_{SRV_{in}}| + |V_{SRV_{out}}|)/\text{diameter}$]; the magnitude of azimuthal shear is half of the rotational shear vorticity in Fig. 19a] in a volume scan experienced a sharp increase after the tornado touchdown and peaked at around 1544 LST at the 2.4° elevation angle with a value of 0.034 s^{-1} . This feature was different from what was observed in the U.S. cases in a statistical work by Grant and Prentice (1996), in which the maximum azimuthal shear increased with time before tornado touchdown, but sharply decreased immediately after that. The maximum rotational velocity (34 m s^{-1}) and azimuthal shear (0.034 s^{-1}) of the Foshan tornadic mesocyclone were both generally greater than those of the tornadic mesocyclones associated with minisupercells in the United States (e.g., Grant and Prentice 1996; Spratt et al. 1997; Schneider and Sharp 2007) and Japan (e.g., Suzuki et al. 2000).

The evolution of the mesocyclone was also evident in 5-min surface wind changes (the 10-m wind detected at each time minus that 5 min earlier). Clear enhancement in the convergent component of the wind vector was observed along the tornado track. The extent of the convergent wind change pattern covered a width of about 8 km around the tornado track between 1525 and 1600 LST (e.g., Figs. 6d–f). It suggests that observations from the mesonet network of in situ surface weather stations could be an important tool for monitoring the near-surface evolution of a mesocyclone.

Tornadic vortex signatures. The evolution of the tornado vortex signature (TVS; American Meteorological Society 2016b) was detected by the Guangzhou radar during this event. The TVS was identified in this study as a cyclonic shear signature with a local maximal gate-to-gate azimuthal radial velocity difference (DV) of at least 20 m s^{-1} over an azimuthal distance of one beamwidth [the same criteria used by Meng and Yao (2014)]. During the life span of the Foshan tornado, the beamwidth at the 0.5° elevation angle of the Guangzhou radar was about 400 m. All TVSs during this event were manually identified based on the Guangzhou and Shenzhen radars. The time of the TVS was determined using the recorded receiving time of the corresponding radar beam.

The TVS was first detected between 1 and 2.2 km AGL about 10 min later than the time when the mesocyclone was first detected. It then developed both downward and upward. The downward development from the middle level has been observed by U.S. WSR-88Ds, while only the upward development from near the surface was observed by the hybrid phased-array Doppler radar and the Mobile Weather Radar (French et al. 2013). By neglecting the data at the 0.5° elevation angle before 1536:55 LST, which were not able to be used because of the range-folded velocity (e.g., Fig. 6d), we found that the strongest TVS occurred at 1536:55 LST at the same volume scan and elevation angle as those of the strongest mesocyclone (Figs. 19d,c). The strength (DV) of the strongest TVS reached 60 m s^{-1} at ~ 420 m AGL. Similar to the sequence of the strongest mesocyclone and surface damage, the most severe damage was observed about 4 min after the peak strength of the low-level TVS. At 1542:41 LST, the 0.5° TVS was located around LYI (Figs. 6f,c) with the DV decreasing to 51.5 m s^{-1} at the 0.5° elevation angle (Fig. 19d). The TVS dramatically weakened at the lowest level at 1548:58 LST and vanished at about 1600 LST. All the identified TVSs were below 3 km AGL during the entire event.

The collocation of the condensation funnel and the TVS location at the 0.5° elevation angle was estimated based on the video information together with the data from the Guangzhou radar. The identified 0.5° TVSs were found to be consistently located on the left side of the tornado centerline relative to the tornado motion with the cross-track deviations of approximately 520, 290, 320, and 250 m at 1530:37, 1536:55, 1542:41, and 1548:58 LST, respectively (e.g., Fig. 6). The mesocyclone center, however, was not always located on the same side as the corresponding TVS (e.g., Fig. 6e). To obtain the along-track deviation, we needed first to determine the tornado

location at the same time of the TVS. For the TVS at JY at 1536:55 LST (Fig. 10a), a traffic surveillance camera (camera 6) about 250 m northeast of it happened to record the passing process of the tornado. According to the variation of the near-surface wind pattern, the time when the tornado crossed the road was 1538:24 LST (Figs. 10a,c). We estimated the translation speed (18.0 m s^{-1}) of the tornado by assuming that the tornado had the same translation speed as that of the TVS from 1530:37 to 1536:55 LST. The horizontal along-track deviation of the TVS at 1536:55 LST from the tornado center was about 1,622 m ahead of the condensation funnel at the ground. The uncertainty was mainly from the estimation of the translation speed of the tornado. By assuming the tornado had a uniform motion during the 32-min life cycle along the damage swath, its translation speed was about 16.1 m s^{-1} . Thus, we assumed that there was an uncertainty of 2 m s^{-1} for the translation speed estimate, and there was an error of $\pm 178 \text{ m}$ for the horizontal along-track deviation of the TVS at 1536:55 LST. The same estimation was applied to the TVS at 1530:37 LST to the south of BAC (Fig. 7a), where the result showed a horizontal along-track deviation of approximately $404 \pm 106 \text{ m}$. These results suggest that the horizontal along-track displacement between the 0.5° TVS and the condensation funnel at the ground experienced an increase before the tornado reached its peak strength.

SUMMARY AND DISCUSSION. This work presented the most detailed analysis on a TC tornado up to now based on ground and aerial damage surveys, and visual, radar, and surface observations, which could become an important addition to those great integrated analyses on midlatitude tornadoes in the literature.

The TC tornado examined in this work occurred in Foshan, Guangdong Province, China, at about 1528 LST 4 Oct 2015. It was generated in a minisupercell $\sim 350 \text{ km}$ to the northeast of the center of the western North Pacific Typhoon Mujigae when the TC made landfall in Zhanjiang, Guangdong Province. Compared to the TC tornadic environment in U.S. climatology, the sounding-derived environmental parameters in the Foshan TC tornado case mainly fell in the high-tornado-threat category.

Our analyses revealed that this TC tornado had many features similar to midlatitude tornadoes. The tornado lasted for 32 min and produced a damage swath 30.85 km long with a maximum width of 570 m, roughly in parallel to the movement of its parent TC rainband. With respect to the tornado

motion, the damage swath had a larger area on the right side of the tornado track than on the left side, likely a result of the overlapping of the northwestward movement of the tornado with its system-relative cyclonic rotation.

Near-surface wind patterns of the tornado revealed by tornado videos were compared to those revealed by fallen trees. They both showed highly convergent flow toward the tornado center near the surface outside the condensation funnel. However, tornado videos showed apparently cyclonic flow both at and above the ground near the condensation funnel, while the fallen trees demonstrated either a cyclonic or convergent pattern near the condensation funnel at the ground.

The diameter of the condensation funnel at the ground was generally smaller than the extent of the EF2 isopleth. A diameter of approximately $13.3 \pm 2 \text{ m}$ was obtained from the tornado video, where the strongest damage that was produced nearby was EF1. The near-surface wind speed, at a spot about 70 m away from the tornado center, was estimated based on the movement of the spray raised by the debris of the tornado. The photogrammetrically derived wind speed estimate provides evidence to support that derived from the EF scale. Tornado videos also revealed the occurrences of vertical subvortices and a horizontal vortex tube, which had been observed in midlatitude tornadoes. One interesting feature of this TC tornadic supercell that has been seldom noticed in midlatitude tornadic supercells was that its overshooting cloud top remained active despite having been ripped apart from the lower part of the supercell, which awaits further investigation.

The strength of the Foshan TC tornado mesocyclone was generally greater than those of tornadic mesocyclones associated with minisupercells in the United States and Japan. The maximum 0.5° peak rotational velocity (34 m s^{-1}) of this EF3 tornado case was close to the median of rotational velocities associated with EF3 tornadoes in the United States. Similar to what was observed by WSR-88Ds in the United States, the TVS initially appeared in the middle level and developed downward. The lowest-level TVSs were consistently located on the left side (also the TC side) of the damage swath relative to the tornado motion with a cross-track deviation of several hundred meters and an along-track deviation of several hundred meters to more than 1,000 m ahead of the condensation funnel at the ground. The TVS attained its lowest-level maximum intensity (gate-to-gate azimuthal radial velocity difference of 60 m s^{-1}) at the same time as that of the maximum intensity of the mesocyclone. The most severe tornado damage occurred about 4 min after

the appearance of the strongest 0.5° mesocyclone and TVS. This information could become useful guidance for tornado warning decision-making.

In addition to presenting a detailed integrated TC tornado case review, this work also provided the most detailed tornado case study with the most comprehensive information of a tornado ever in the history of China. Likely because of the low frequency of tornadoes (about one-tenth of the frequency in the United States; Fan and Yu 2015), research on tornadoes—especially on damage surveys in China—were not paid much attention. Damage surveys had mainly just involved taking several pictures of the most severely damaged structures. In recent years—especially after the occurrence of the shipwreck of the *Oriental Star* in the Yangtze River on 1 June 2015, which was associated with a microburst that claimed 442 lives (Meng et al. 2016), and the Yancheng, Jiangsu Province, EF4 tornado on 23 June 2016, which claimed 99 lives (Xue et al. 2016)—the China Meteorological Administration initiated the establishment of a set of operational policies for strong wind damage surveys, and quasi-operational tests for monitoring tornadoes and issuing tornado warnings at five meteorological agencies where there had been high tornado frequency such as Jiangsu and Guangdong provinces.

Concerning the validation of using the EF scale, which is based on construction codes in the United States, in this Chinese case study as in most tornado damage survey studies outside the United States, this work compared the main differences between building construction in China and the United States. General similarities were found in factories, warehouses, and tall buildings. Trees and transmission towers or poles can be regarded as the same. Consequently, many EF-scale DIs can be directly used with acceptable uncertainties and such uncertainties can be well accounted for by using the expected value of the estimated wind speed range as in the EFkit. In this sense, this study provides another case demonstrating the validation in applying the EF scale for tornado damage surveys to a place outside the United States. Currently, scientists in the Chinese Academy of Meteorological Sciences (CAMS) are trying to develop local DIs based on the construction codes for different places in China for more reasonable wind estimation. All these efforts will not only be helpful in establishing more accurate tornado records in China but also in improving people's awareness of the state of the art of worldwide extreme weather events.

ACKNOWLEDGMENTS. We thank the Foshan Meteorological Service, especially Dr. Jianjun Zhu, for mak-

ing the aerial damage survey possible. Special thanks go to all of the photographers who shared their valuable pictures and videos of the tornado and its damage. We also thank the editor and three anonymous reviewers for their valuable constructive suggestions. L. Bai, Z. Meng, L. Huang, Y. Huang, and D. Yao were supported by the National Key Basic Research and Development Project of China Grant 2013CB430104; L. Bai, Z. Meng, L. Huang, and D. Yao were also supported by the Natural Science Foundation of China Grants 41425018, 41375048, and 41461164006; Z. Li was supported by the Guangdong Meteorological Service Science Technology Research Program Grant 2014B21.

REFERENCES

- American Meteorological Society, 2016a: Mesocyclone. Glossary of Meteorology, <http://glossary.ametsoc.org/wiki/Mesocyclone>.
- , 2016b: Tornadic vortex signature. Glossary of Meteorology, http://glossary.ametsoc.org/wiki/Tornadic_vortex_signature.
- Atkins, N. T., K. M. Butler, K. R. Flynn, and R. M. Wakimoto, 2014: An integrated damage, visual, and radar analysis of the 2013 Moore Oklahoma EF5 tornado. *Bull. Amer. Meteor. Soc.*, **95**, 1549–1561, <https://doi.org/10.1175/BAMS-D-14-00033.1>.
- Bluestein, H. B., J. C. Snyder, J. B. Houser, and A. L. Pazmany, 2012: Rapid-scan, polarimetric, Doppler-radar observations of an EF-5 tornado in Oklahoma on 24 May 2011. Preprints, *26th Conf. on Severe Local Storms*, Nashville, TN, Amer. Meteor. Soc., 16.3, <https://ams.confex.com/ams/26SLS/webprogram/Paper212022.html>.
- Bodine, D., M. Kumjian, R. Palmer, P. Heinselman, and A. Ryzhkov, 2013: Tornado damage estimation using polarimetric radar. *Wea. Forecasting*, **28**, 139–158, <https://doi.org/10.1175/WAF-D-11-00158.1>.
- Edwards, R., 2012: Tropical cyclone tornadoes: A review of knowledge in research and prediction. *Electron. J. Severe Storms Meteor.*, **7** (6), www.ejssm.org/ojs/index.php/ejssm/issue/view/39.
- , A. Dean, R. Thompson, and B. Smith, 2012: Convective modes for significant severe thunderstorms in the contiguous United States. Part III: Tropical cyclone tornadoes. *Wea. Forecasting*, **27**, 1507–1519, <https://doi.org/10.1175/WAF-D-11-00117.1>.
- Fan, W., and X. Yu, 2015: Characteristics of spatial-temporal distribution of tornadoes in China (in Chinese with English abstract). *Meteor. Mon.*, **41**, 793–805.
- Fang, L., J. Ji, G. Tao, C. Zhou, and K. Wang, 2009: Weather analysis and grade determination of a tornado occurring in a single super-storm (in Chinese with English abstract). *J. Nat. Disasters*, **2**, 167–172.

- French, M., H. Bluestein, I. PopStefanija, C. Baldi, and R. Bluth, 2013: Reexamining the vertical development of tornadic vortex signatures in supercells. *Mon. Wea. Rev.*, **141**, 4576–4601, <https://doi.org/10.1175/MWR-D-12-00315.1>.
- Gentry, R. C., 1983: Genesis of tornadoes associated with hurricanes. *Mon. Wea. Rev.*, **111**, 1793–1805, [https://doi.org/10.1175/1520-0493\(1983\)111<1793:GOTAWH>2.0.CO;2](https://doi.org/10.1175/1520-0493(1983)111<1793:GOTAWH>2.0.CO;2).
- Grant, B. N., and R. Prentice, 1996: Mesocyclone characteristics of mini supercell thunderstorms. Preprints, *15th Conf. on Weather Analysis and Forecasting*, Norfolk, VA, Amer. Meteor. Soc., 362–365.
- Hill, E., W. Malkin, and J. W. A. Schultz, 1966: Tornadoes associated with cyclones of tropical origin—Practical features. *J. Appl. Meteor.*, **5**, 745–763, [https://doi.org/10.1175/1520-0450\(1966\)005<0745:TAWCOT>2.0.CO;2](https://doi.org/10.1175/1520-0450(1966)005<0745:TAWCOT>2.0.CO;2).
- Houser, J., H. Bluestein, and J. Snyder, 2016: A finescale radar examination of the tornadic debris signature and weak-echo reflectivity band associated with a large, violent tornado. *Mon. Wea. Rev.*, **144**, 4101–4130, <https://doi.org/10.1175/MWR-D-15-0408.1>.
- Huang, X., L. Yan, S. Wang, and Z. Cheng, 2014: Analysis of the characteristics of tornados in Foshan City and their circulation background (in Chinese with English abstract). *Guangdong Meteor.*, **36**, 20–24.
- Knupp, K., and Coauthors, 2014: Meteorological overview of the devastating 27 April 2011 tornado outbreak. *Bull. Amer. Meteor. Soc.*, **95**, 1041–1062, <https://doi.org/10.1175/BAMS-D-11-00229.1>.
- LaDue, J. G., and E. A. Mahoney, 2006: Implementing the new enhanced Fujita scale within the NWS. *23rd Conf. on Severe Local Storms*, St. Louis, MO, Amer. Meteor. Soc., 5.5, https://ams.confex.com/ams/23SLS/techprogram/paper_115420.htm.
- Li, Y., L. Chen, and S. Zhang, 2004: Statistical characteristics of tropical cyclone making landfalls on China (in Chinese with English abstract). *J. Trop. Meteor.*, **62**, 541–549.
- Lin, Z., 1995: Damage survey on “6.9” tornadoes in Nanhai and Guangzhou (in Chinese). *Guangdong Meteor.*, **7**, 36–38.
- Mashiko, W., H. Niino, and T. Kato, 2009: Numerical simulation of tornadogenesis in an outer-rainband minisupercell of Typhoon Shanshan on 17 September 2006. *Mon. Wea. Rev.*, **137**, 4238–4260, <https://doi.org/10.1175/2009MWR2959.1>.
- McCaul, B., and B. Hagemeyer, 2016: Are TC tornadoes weaker than midlatitude tornadoes? NOAA/AOML Hurricane Research Division, www.aoml.noaa.gov/hrd/tcfaq/L6.html.
- McCaul, E. W., Jr., 1991: Buoyancy and shear characteristics of hurricane-tornado environments. *Mon. Wea. Rev.*, **119**, 1954–1978, [https://doi.org/10.1175/1520-0493\(1991\)119<1954:BASCOH>2.0.CO;2](https://doi.org/10.1175/1520-0493(1991)119<1954:BASCOH>2.0.CO;2).
- , and M. L. Weisman, 1996: Simulations of shallow supercell storms in landfalling hurricane environments. *Mon. Wea. Rev.*, **124**, 408–429, [https://doi.org/10.1175/1520-0493\(1996\)124<0408:SOSSSI>2.0.CO;2](https://doi.org/10.1175/1520-0493(1996)124<0408:SOSSSI>2.0.CO;2).
- , D. E. Buechler, S. J. Goodman, and M. Cammarata, 2004: Doppler radar and lightning network observations of a severe outbreak of tropical cyclone tornadoes. *Mon. Wea. Rev.*, **132**, 1747–1763, [https://doi.org/10.1175/1520-0493\(2004\)132<1747:DRALNO>2.0.CO;2](https://doi.org/10.1175/1520-0493(2004)132<1747:DRALNO>2.0.CO;2).
- Meng, Z., and D. Yao, 2014: Damage survey, radar, and environment analyses on the first-ever documented tornado in Beijing during the heavy rainfall event of 21 July 2012. *Wea. Forecasting*, **29**, 702–724, <https://doi.org/10.1175/WAF-D-13-00052.1>.
- , and Coauthors, 2016: Wind estimation around the shipwreck of Oriental Star based on field damage surveys and radar observations. *Sci. Bull.*, **61**, 330–337, <https://doi.org/10.1007/s11434-016-1005-2>.
- Moore, T. W., and R. Dixon, 2011: Climatology of tornadoes associated with Gulf Coast-landfalling hurricanes. *Geogr. Rev.*, **101**, 371–395, <https://doi.org/10.1111/j.1931-0846.2011.00102.x>.
- Morin, M. J., M. D. Parker, K. A. Hill, and G. M. Lackmann, 2010: A numerical investigation of supercells in landfalling tropical cyclones. *25th Conf. on Severe Local Storms*, Denver, CO, Amer. Meteor. Soc., P3.3, <https://ams.confex.com/ams/25SLS/webprogram/Paper175965.html>.
- Mou, Z., C. Zhang, and X. Pan, 2001: A damage survey of the tornado first captured by meteorological instrument in Zhejiang China (in Chinese with English abstract). *J. Zhejiang Meteor.*, **22**, 41–43.
- Novlan, D. J., and W. M. Gray, 1974: Hurricane-spawned tornadoes. *Mon. Wea. Rev.*, **102**, 476–488, [https://doi.org/10.1175/1520-0493\(1974\)102<0476:HST>2.0.CO;2](https://doi.org/10.1175/1520-0493(1974)102<0476:HST>2.0.CO;2).
- Orf, L., R. Wilhelmson, B. Lee, C. Finley, and A. Houston, 2017: Evolution of a long-track violent tornado within a simulated supercell. *Bull. Amer. Meteor. Soc.*, **98**, 45–68, <https://doi.org/10.1175/BAMS-D-15-00073.1>.
- Rao, G. V., J. W. Scheck, R. Edwards, and J. T. Schaefer, 2005: Structures of mesocirculations producing tornadoes associated with Tropical Cyclone Frances (1998). *Pure Appl. Geophys.*, **162**, 1627–1641, <https://doi.org/10.1007/s00024-005-2686-7>.
- Schneider, D., and S. Sharp, 2007: Radar signatures of tropical cyclone tornadoes in central North

- Carolina. *Wea. Forecasting*, **22**, 278–286, <https://doi.org/10.1175/WAF992.1>.
- Schultz, L. A., and D. J. Cecil, 2009: Tropical cyclone tornadoes, 1950–2007. *Mon. Wea. Rev.*, **137**, 3471–3484, <https://doi.org/10.1175/2009MWR2896.1>.
- Smith, B., R. Thompson, A. Dean, and P. Marsh, 2015: Diagnosing the conditional probability of tornado damage rating using environmental and radar attributes. *Wea. Forecasting*, **30**, 914–932, <https://doi.org/10.1175/WAF-D-14-00122.1>.
- Smith, J. S., 1965: The hurricane-tornado. *Mon. Wea. Rev.*, **93**, 453–459, [https://doi.org/10.1175/1520-0493\(1965\)093<0453:THT>2.3.CO;2](https://doi.org/10.1175/1520-0493(1965)093<0453:THT>2.3.CO;2).
- Spratt, S. M., D. W. Sharp, P. Welsh, A. C. Sandrik, F. Alsheimer, and C. Paxton, 1997: A WSR-88D assessment of tropical cyclone outer rainband tornadoes. *Wea. Forecasting*, **12**, 479–501, [https://doi.org/10.1175/1520-0434\(1997\)012<0479:AWAOTC>2.0.CO;2](https://doi.org/10.1175/1520-0434(1997)012<0479:AWAOTC>2.0.CO;2).
- Suzuki, O., H. Niino, H. Ohno, and H. Nirasawa, 2000: Tornado-producing mini supercells associated with Typhoon 9019. *Mon. Wea. Rev.*, **128**, 1868–1882, [https://doi.org/10.1175/1520-0493\(2000\)128<1868:TPMSAW>2.0.CO;2](https://doi.org/10.1175/1520-0493(2000)128<1868:TPMSAW>2.0.CO;2).
- Tao, Y., C. Yu, F. Zhang, D. Li, and J. Liu, 2016: Major heavy rain events in China from April to October in 2015 (in Chinese with English abstract). *Torrential Rain Disasters*, **35**, 187–196.
- Thompson, R. L., R. Edwards, J. A. Hart, K. L. Elmore, and P. Markowski, 2003: Close proximity soundings within supercell environments obtained from the Rapid Update Cycle. *Wea. Forecasting*, **18**, 1243–1261, [https://doi.org/10.1175/1520-0434\(2003\)018<1243:CPSWSE>2.0.CO;2](https://doi.org/10.1175/1520-0434(2003)018<1243:CPSWSE>2.0.CO;2).
- Tucker, R. W., 2016: How do the building codes and standards in China compare with those in the U.S.? Dodge Data & Analytics, www.construction.com/InternationalCenter/AsktheExperts/ask_121703.asp.
- Verbout, S. M., D. M. Schultz, L. M. Leslie, H. E. Brooks, D. J. Karoly, and K. L. Elmore, 2007: Tornado outbreaks associated with landfalling hurricanes in the North Atlantic Basin: 1954–2004. *Meteor. Atmos. Phys.*, **97**, 255–271, <https://doi.org/10.1007/s00703-006-0256-x>.
- Wakimoto, R. M., H. V. Murphey, D. C. Dowell, and H. B. Bluestein, 2003: The Kellerville tornado during VORTEX: Damage survey and Doppler radar analyses. *Mon. Wea. Rev.*, **131**, 2197–2221, [https://doi.org/10.1175/1520-0493\(2003\)131<2197:TKTDV D>2.0.CO;2](https://doi.org/10.1175/1520-0493(2003)131<2197:TKTDV D>2.0.CO;2).
- , and Coauthors, 2016: Aerial damage survey of the 2013 El Reno tornado combined with mobile radar data. *Mon. Wea. Rev.*, **144**, 1749–1776, <https://doi.org/10.1175/MWR-D-15-0367.1>.
- Weiss, S. J., 1987: Some climatological aspects of forecasting tornadoes associated with tropical cyclones. Preprints, *17th Conf. on Hurricanes and Tropical Meteor.*, Miami, FL, Amer. Meteor. Soc., 160–163.
- WSEC, 2006: A recommendation for an enhanced Fujita scale (EF-scale). Texas Tech University Wind Science and Engineering Center Rep., 111 pp, www.depts.ttu.edu/nwi/Pubs/FSscale/EFScale.pdf.
- Xue, M., K. Zhao, M. Wang, Z. Li, and Y. Zheng, 2016: Recent significant tornadoes in China. *Adv. Atmos. Sci.*, **33**, 1209–1217, <https://doi.org/10.1007/s00376-016-6005-2>.
- Yang, Z., and S. Gao, 2016: Analysis of the October 2015 atmospheric circulation and weather (in Chinese with English abstract). *Meteor. Mon.*, **42**, 122–128.
- Zhao, K., and Coauthors, 2017: Doppler radar analysis of a tornadic miniature supercell during the landfall of Typhoon Mujigae (2015) in south China. *Bull. Amer. Meteor. Soc.*, <https://doi.org/10.1175/BAMS-D-15-00301.1>, in press.
- Zheng, F., 2009: A strong tornado in the outer-region of the super typhoon “Sepat” in 2007 (in Chinese with English abstract). *Zhongguo Nongxue Tongbao*, **25**, 283–286.
- Zheng, Y., B. Zhang, X. Wang, K. Sun, R. Mu, and W. Xia, 2015: Analysis of typhoon-tornado weather background and radar echo structure (in Chinese with English abstract). *Meteor. Mon.*, **41**, 942–952.
- Zhu, X., and J. Zhu, 2004: New generation weather radar network in China (in Chinese with English abstract). *Meteor. Sci. Technol.*, **32**, 255–258.